

Structure deformation and curvature sensing of PIEZO1 in lipid membranes

<https://doi.org/10.1038/s41586-022-04574-8>

Xuzhong Yang^{1,5}, Chao Lin^{2,5}, Xudong Chen^{1,5}, Shouqin Li^{2,3,4,5}, Xueming Li^{2,5} & Bailong Xiao^{1,5}

Received: 6 December 2021

Accepted: 23 February 2022

Published online: 6 April 2022

 Check for updates

PIEZO channels respond to piconewton-scale forces to mediate critical physiological and pathophysiological processes^{1–5}. Detergent-solubilized PIEZO channels form bowl-shaped trimers comprising a central ion-conducting pore with an extracellular cap and three curved and non-planar blades with intracellular beams^{6–10}, which may undergo force-induced deformation within lipid membranes¹¹. However, the structures and mechanisms underlying the gating dynamics of PIEZO channels in lipid membranes remain unresolved. Here we determine the curved and flattened structures of PIEZO1 reconstituted in liposome vesicles, directly visualizing the substantial deformability of the PIEZO1–lipid bilayer system and an in-plane areal expansion of approximately 300 nm² in the flattened structure. The curved structure of PIEZO1 resembles the structure determined from detergent micelles, but has numerous bound phospholipids. By contrast, the flattened structure exhibits membrane tension-induced flattening of the blade, bending of the beam and detaching and rotating of the cap, which could collectively lead to gating of the ion-conducting pathway. On the basis of the measured in-plane membrane area expansion and stiffness constant of PIEZO1 (ref. ¹¹), we calculate a half maximal activation tension of about 1.9 pN nm⁻¹, matching experimentally measured values. Thus, our studies provide a fundamental understanding of how the notable deformability and structural rearrangement of PIEZO1 achieve exquisite mechanosensitivity and unique curvature-based gating in lipid membranes.

PIEZO channels are mechanically activated cation channels with exquisite mechanosensitivity^{1,2}. For instance, PIEZO1 can intrinsically respond to changes in membrane tension³ with a measured half-maximal activation tension (T_{50}) of about 1.4 mN m⁻¹ (equivalent to 1.4 pN nm⁻¹). This high mechanosensitivity may enable PIEZO channels to serve as versatile mechanotransducers in various cell types and consequently mediate many essential physiological processes^{4,12}. For instance, PIEZO1 is required for cardiovascular development and function^{13–15}, blood pressure regulation^{16,17}, bone formation and remodelling¹⁸, red blood cell volume regulation¹⁹ and innate immunity²⁰, and PIEZO2 has a dominant role in the somatosensory neurons mediating gentle touch, proprioception, interoception and tactile pain^{21–28}. Mutations in *PIEZO1* and *PIEZO2* have been associated with various forms of human genetic diseases, demonstrating their clinical relevance and validity as novel therapeutic targets⁴.

PIEZO channels form a propeller-shaped homotrimer^{6–10}. The unusually curved arrangement of the 38 transmembrane helices in each of the 3 subunits (Extended Data Fig. 1a) collectively shapes a signature nano-bowl configuration in the membrane plane⁷. PIEZO1 reconstituted in liposome vesicles has been shown to curve the residing membrane and undergo reversible flattening at biologically relevant forces, leading to the proposal that PIEZO channels use a structure-based

membrane dome mechanism, accounting for their extraordinary mechanosensitivity^{10,11}. To test this curvature-based gating mechanism, we aimed to determine both the curved and flattened structures of PIEZO1 reconstituted in liposomes, enabling us to directly analyse the structural dynamics of PIEZO1 in lipid membranes.

Structural determination in liposomes

As described in detail in Methods and shown in the workflow (Fig. 1a), we explored experimental conditions to achieve efficient proteoliposome reconstitution of mouse PIEZO1 and homogenous size of the liposome vesicles suitable for single-particle cryo-electron microscopy (cryo-EM) structure determination (Extended Data Fig. 1b–j). The majority of PIEZO1 channels were preferentially reconstituted into the liposomes in an outside-in configuration, in which the featured extracellular cap domain is located inside the lipid vesicles (Fig. 1b). We imaged approximately 780,000 such outside-in vesicles, enabling us to determine the structure of the curved state of PIEZO1 at a resolution of 3.46 Å (Fig. 2a–d, Extended Data Figs. 3–5, Extended Data Table 1). Notably, a few proteoliposomes with PIEZO1 in the outside-out orientation were observed in the Quantifoil grid samples (Fig. 1b). We collected approximately 35,000 micrographs to obtain around 120,000 particles for

¹State Key Laboratory of Membrane Biology, Tsinghua-Peking Center for Life Sciences, IDG/McGovern Institute for Brain Research, School of Pharmaceutical Sciences, Beijing Frontier Research Center for Biological Structure, Beijing Advanced Innovation Center for Structural Biology, Tsinghua University, Beijing, China. ²MOE Key Laboratory of Protein Sciences, Beijing Frontier Research Center for Biological Structure, Beijing Advanced Innovation Center for Structural Biology, Tsinghua-Peking Center for Life Sciences, School of Life Sciences, Tsinghua University, Beijing, China. ³Institute of Physics, Chinese Academy of Sciences, Beijing, China. ⁴University of Chinese Academy of Sciences, Beijing, China. ⁵These authors contributed equally: Xuzhong Yang, Chao Lin, Xudong Chen, Shouqin Li. [✉]e-mail: lixueming@tsinghua.edu.cn; xbailong@mail.tsinghua.edu.cn

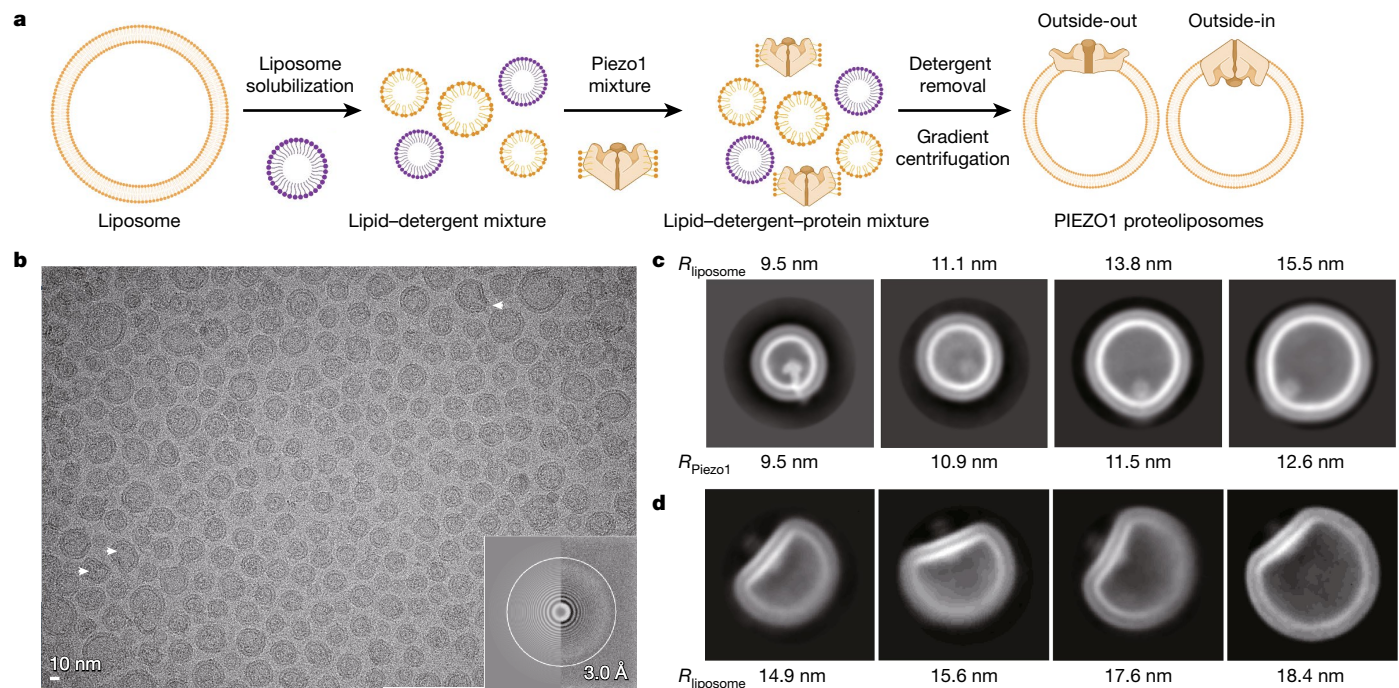


Fig. 1 | Cryo-EM structure determination of PIEZO1 proteoliposomes and analyses of PIEZO1-membrane deformation. **a**, Workflow for the preparation of PIEZO1 proteoliposomes for cryo-EM structure determination. **b**, A representative cryo-EM micrograph of PIEZO1 proteoliposomes on a Quantifoil Au grid. The power spectrum with the 3.0 Å frequency indicated is shown in the bottom right corner of the micrograph. The rarely observed D-shaped proteoliposome vesicles are indicated by the arrow. **c**, Two-dimensional

average images of liposome vesicles of different sizes with PIEZO1 reconstituted in the outside-in configuration. The calculated radii of the PIEZO1-residing side indicated by the cap domain (R_{Piezo1}) and the opposite pole (R_{liposome}) of the same vesicle are labelled. **d**, Two-dimensional average images of the D-shaped liposome vesicles of different sizes with PIEZO1 reconstituted in the outside-out configuration. The measured liposome size is shown.

determining the flattened structure with 26 resolved transmembrane helices at a medium resolution (Fig. 2e–g, Extended Data Figs. 6, 7, Extended Data Table 1).

Deformation of the PIEZO1-membrane system

Compared with the empty liposomes with smooth and rounded surfaces (Extended Data Fig. 2b), the PIEZO1 proteoliposomes were irregular and twisted (Fig. 1b, Extended Data Fig. 2a). Two-dimensional average images show that the proteoliposomes appear as a droplet shape in which PIEZO1 prefers a cap-inside orientation to match its curvature with the shape of liposomes (Fig. 1c). For proteoliposomes of different sizes, we calculated the curvature radius of the PIEZO1-residing pole (R_{Piezo1}) and the opposite pole of the same liposome (R_{liposome}) (Fig. 1c, Extended Data Fig. 2c). The bowl-shaped PIEZO1 structure derived from detergent micelles was estimated¹⁰ to have a curvature radius of approximately 10.2 nm, which may be free of membrane tension and therefore represent an energetically favoured state. Indeed, R_{Piezo1} is nearly equal to R_{liposome} when PIEZO1 is reconstituted into liposome vesicles, with R_{liposome} ranging between 9.5 nm and 11.1 nm (Fig. 1c), indicating a curvature with an average radius of 10 nm for both PIEZO1 and the liposome at equilibrium and, consequently, a minimal tension on the PIEZO1 channel. By contrast, for liposomes with R_{liposome} larger than 11 nm, R_{Piezo1} is smaller than R_{liposome} (Fig. 1c, Extended Data Fig. 2c), indicating PIEZO1-induced deformation of the membrane. Furthermore, the residing PIEZO1 displayed considerable flexible conformations (Fig. 1c, Extended Data Fig. 2c). The relatively homogenous class of proteoliposomes with a R_{liposome} of approximately 10 nm eventually led us to determine the structure of PIEZO1 in the curved conformation (Extended Data Fig. 3a–c).

For proteoliposomes with PIEZO1 reconstituted in an outside-out configuration, 2D average images show that PIEZO1 and the residing membrane are completely flattened, whereas the opposite pole retains the vesicle curvature, resulting in D-shaped proteoliposomes, independent of the vesicle size (Fig. 1d). The curvature mismatch between the flattened PIEZO1-residing membrane and the rest of the curved vesicle may impose much greater membrane tension and bending force on PIEZO1 than in the cap-inside configuration, suggesting that forces derived from the lipid membrane alone are sufficient to drive PIEZO1 from the curved state to a fully flattened state. The small number of the D-shaped proteoliposomes is consistent with an energetically unfavourable state.

Curved structure in lipid membranes

The density map of the droplet-shaped proteoliposome shows PIEZO1 embedded in the liposome, with 22 resolved transmembrane helices spanning across the simultaneously resolved lipid bilayer and the cap domain inside the vesicle (Fig. 2a, Extended Data Fig. 3d, e). The projected map shows that the embedded PIEZO1 trimer has a radius of 10 nm and the cap has a height of 10 nm (Fig. 2b). The modelled structure essentially resembles those derived from detergent preparations, and has a similar pore radius (Fig. 2c, Extended Data Fig. 3g, h). The structural similarity is consistent with the idea that PIEZO1 reconstituted in the curvature-conformed liposome vesicles with a R_{liposome} of approximately 10 nm experiences a minimal membrane tension as it does in detergent micelles. Notably, eight phospholipids—which we designate ‘blade lipids’—were identified at the boundary crevices of transmembrane helical unit (THU)7 to THU9 (transmembrane helix (TM)25 to TM36) (Fig. 2d, Extended Data Figs. 3i, 5b). The regular insertion at the boundary of neighbouring THUs suggests the presence of

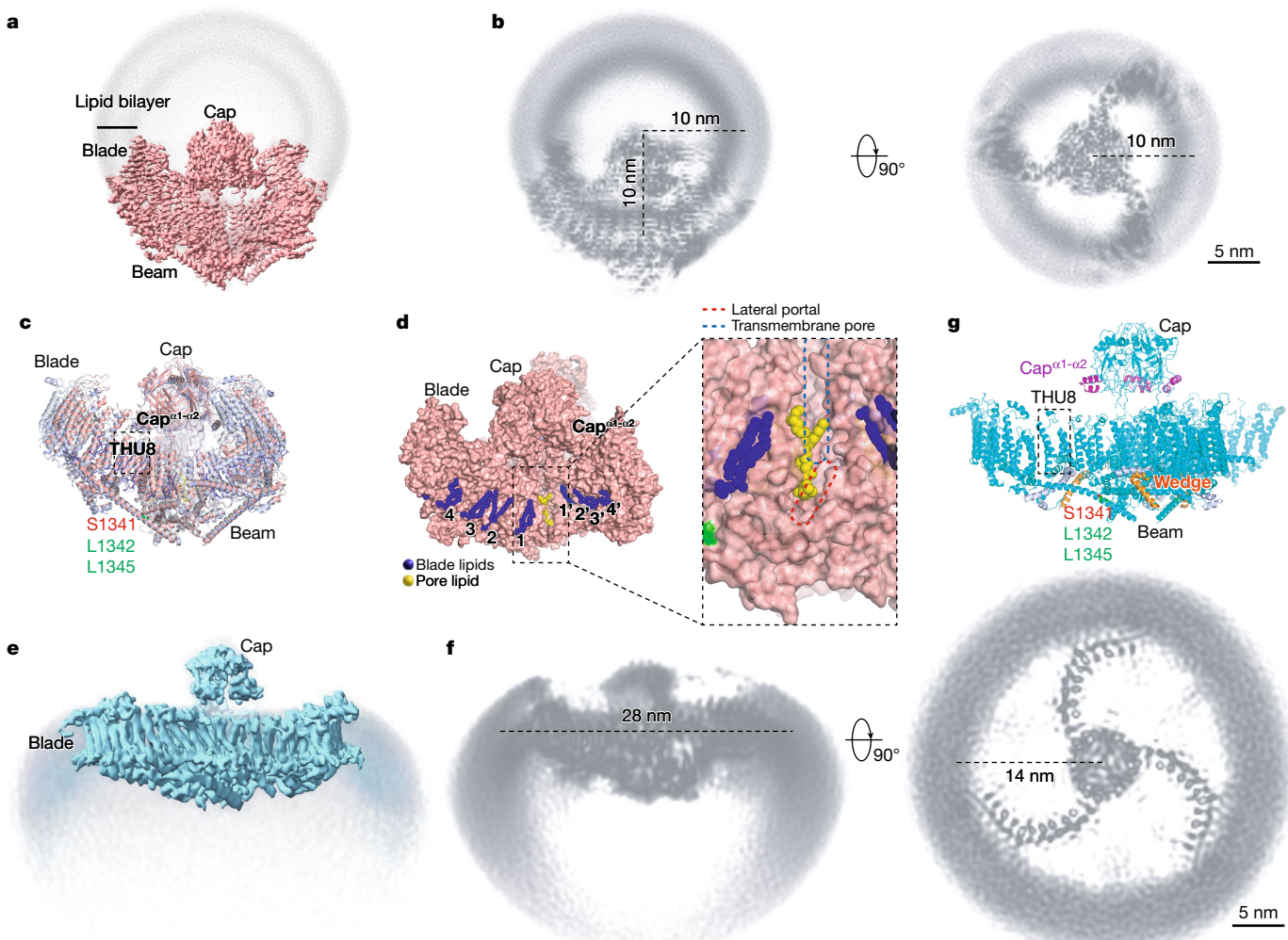


Fig. 2 | Curved and flattened structures of PIEZO1 in liposome vesicles.

a, Side view of the 3D density map of the PIEZO1 proteoliposome with the lipid bilayer of the vesicle displayed in greyscale and the embedded PIEZO1 (at a contour level of 5σ) shown in salmon red. **b**, Projected views of the density map of the PIEZO1 proteoliposome. The radius and height of the embedded PIEZO1 is labelled. **c**, The side view of the overlaid cartoon models of PIEZO1 derived from either proteoliposomes (salmon red) or detergent micelles (Protein Data Bank (PDB) ID: 5Z10 (grey) or 6B3R (light blue)). The modelled phospholipids are shown in blue and yellow. The attachment of the cap to the blade via the interaction between the cap $\alpha 1$ -helix and the extracellular loop of the THU8 is illustrated. The three residues in the beam are labelled in green and red. **d**, Side

view of the surface representation of the PIEZO1 structure showing the 8 blade lipids located on opposite sides of a blade (blue) and the pore lipid (yellow). The enlarged view of the pore lipid illustrates its position close to the indicated central transmembrane pore and lateral portal. **e**, The indicated views of the 3D density map of the PIEZO1 proteoliposome with the lipid bilayer of the vesicle in greyscale and the co-planar PIEZO1 in cyan. **f**, Projected views of the density map of the PIEZO1 proteoliposome. The radius of the embedded PIEZO1 is shown. **g**, Side view of the cartoon model of the flattened PIEZO1 structure. The featured domains are labelled. The detachment of the cap caused by the disrupted interaction between the cap $\alpha 1$ - $\alpha 2$ -helix and the extracellular loop of THU8 is illustrated.

additional unresolved phospholipids at the distal part of the blades comprising THU1 to THU6 (TM1 to TM24) (Extended Data Fig. 1a). These blade phospholipids may therefore serve as structural lipids to stabilize the highly curved blades. An additional phospholipid was observed at the cavity space formed by the outer helix (TM37) and inner helix (TM38) (Fig. 2d, Extended Data Figs. 3i, 5c), where its hydrophobic fatty acid tails may help to seal the cavity formed in between two neighbouring inner helices or even extend into the transmembrane pore, and its hydrophilic phosphate group head sits immediately above the lateral ion-conducting portal (Fig. 2d, Extended Data Fig. 3i). Given its position and potential to be directly engaged in gating the ion-conducting pore, we call this phospholipid the ‘pore lipid’.

PIEZO1 structures determined in either liposomes or detergents do not resolve the N-terminal region consisting of the first 16 or 12 transmembrane helices, indicating the intrinsic flexibility of the distal blade even within the lipid membrane environment. Inspection of the

2D images of the droplet-shaped PIEZO1 proteoliposomes revealed the boundary point near the middle of the vesicle, where the curvatures of the PIEZO1-residing side and the opposite side are mismatched (Extended Data Fig. 3a). These structural features indicate that the unresolved distal blades may reach a height of around 10 nm, consistent with the measured height of the PIEZO2 structure with 38 completely resolved transmembrane helices⁷ or the complete PIEZO1 structure prediction from AlphaFold2²⁹ (Extended Data Fig. 6d).

Flattened structure in lipid membranes

Three-dimensional reconstruction (Extended Data Fig. 7) of the D-shaped PIEZO1 proteoliposomes (Fig. 1b, d) shows a flattened structure, with 26 resolved transmembrane helices residing in the planar lipid bilayer and all other featured domains observed in the curved structures (Fig. 2e, f, Extended Data Fig. 6a–c). Using the PIEZO1 models

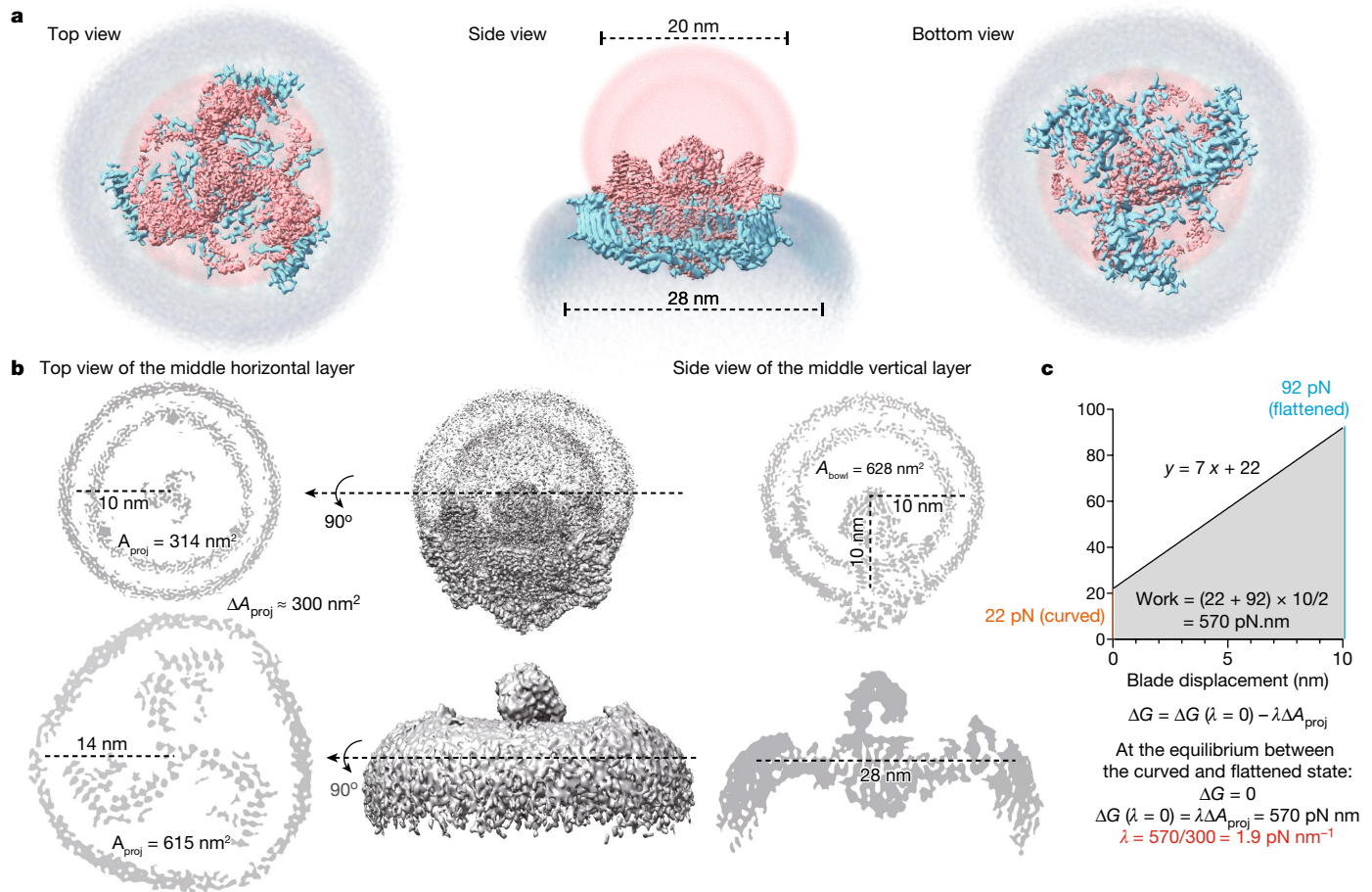


Fig. 3 | In-plane membrane area expansion of the PIEZO1-membrane system. **a**, Indicated views of the superimposed curved (salmon red) and flattened (cyan) PIEZO1 proteoliposomes. The diameter of the projected in-plane membrane area is shown. **b**, Indicated cut-away views of either the middle horizontal layer or the middle vertical layer showing the indicated radii, the projected in-plane membrane area (A_{proj}) and the bowl surface area (A_{bowl}).

c, The previously determined displacement–force linear regression curve and equation¹¹ was adapted to calculate the force and work (the grey area under the curve) required to convert PIEZO1 from the curved to the flattened state. The procedure for calculating the membrane tension (λ) required to obtain equilibrium between the two states is presented.

of the curved structures^{8,10}, we were able to model the flattened structure (Fig. 2g). Compared with the curved structure, there is a distinct wedge-like domain, which is predicted by AlphaFold2 to correspond to residues 1437–1468, following the beam and lateral plug domains (Fig. 2g, Extended Data Figs. 1a, 6d, e). It is likely that flattening the beam domain allows the wedge domain to become ordered. The blades are fully flattened in the z -axis but remain the curved propeller-like shape in the membrane plane when viewed from the top (Fig. 2g, Extended Data Fig. 6e). Furthermore, we identified the pore lipid but not the other eight blade lipids (Extended Data Figs. 5d, 6h), suggesting that phospholipids might adapt the conformational change for interaction.

PIEZO1-membrane expansion

In-plane area expansion of the PIEZO-membrane system has been proposed to determine the mechanosensitivity of PIEZO channels^{7–10}. Taking advantage of the co-resolved lipid bilayers of the proteoliposome vesicles, we directly measured and compared the nano-bowl surface area and the projected in-plane area of the outside-in PIEZO1 liposome and the co-planar outside-out PIEZO1 liposome (Fig. 3a, b). As described above (Extended Data Fig. 3a), the nano-bowl shape of the full structure of PIEZO1 has a depth of 10 nm, perfectly matching the 10-nm radius of the lipid vesicle (Fig. 3b). This gives rise to a nano-bowl surface area of 628 nm^2 and an in-plane projection area of 314 nm^2 (Fig. 3b). The co-planar PIEZO1 membrane of the outside-out PIEZO1 liposome

has a radius of 14 nm and an area of 615 nm^2 , matching the nano-bowl surface area of the outside-in PIEZO1 liposome (Fig. 3b). Thus, the membrane stored in the nano-bowl surface area of the curved PIEZO1 liposome was fully expanded into the in-plane area of the co-planar PIEZO1 membrane in the flattened structure, resulting in an in-plane area expansion of approximately 300 nm^2 upon transition from the curved to the fully flattened state.

Previous studies have determined the force-induced displacement of the blade and obtained the linear regression equation of $y = 7.0x + 22$ (Fig. 3c), where y is the applied force and x is the displacement of the blade¹¹. According to this equation, upon complete flattening of PIEZO1, a 10-nm displacement of the blade would require a mechanical force of approximately 92 nN and work of about 570 pN nm (the grey area under the curve in Fig. 3c). Consider the free energy equation $\Delta G = \Delta G(\lambda = 0) - \lambda \Delta A$, where ΔG and $\Delta G(\lambda = 0)$ are the free energy difference between the curved and flattened state with or without applied tension (λ) and ΔA is the in-plane area change. At equilibrium, ΔG equals 0, leading to $\Delta G(\lambda = 0) = \lambda \Delta A = 570 \text{ pN nm}$, where ΔA is 300 nm^2 , as measured in Fig. 3b. Thus, $\lambda = (570 \text{ pN nm})/(300 \text{ nm}^2) = 1.9 \text{ pN nm}^{-1}$, which matches the experimentally measured value of T_{50} of 1.4 pN.nm^{-1} for PIEZO1 channels³.

Flatten blade-beam to gate lateral plug

Compared with the curved structures derived from both liposomes and detergents, the distal THU4 of the flattened structure expands around

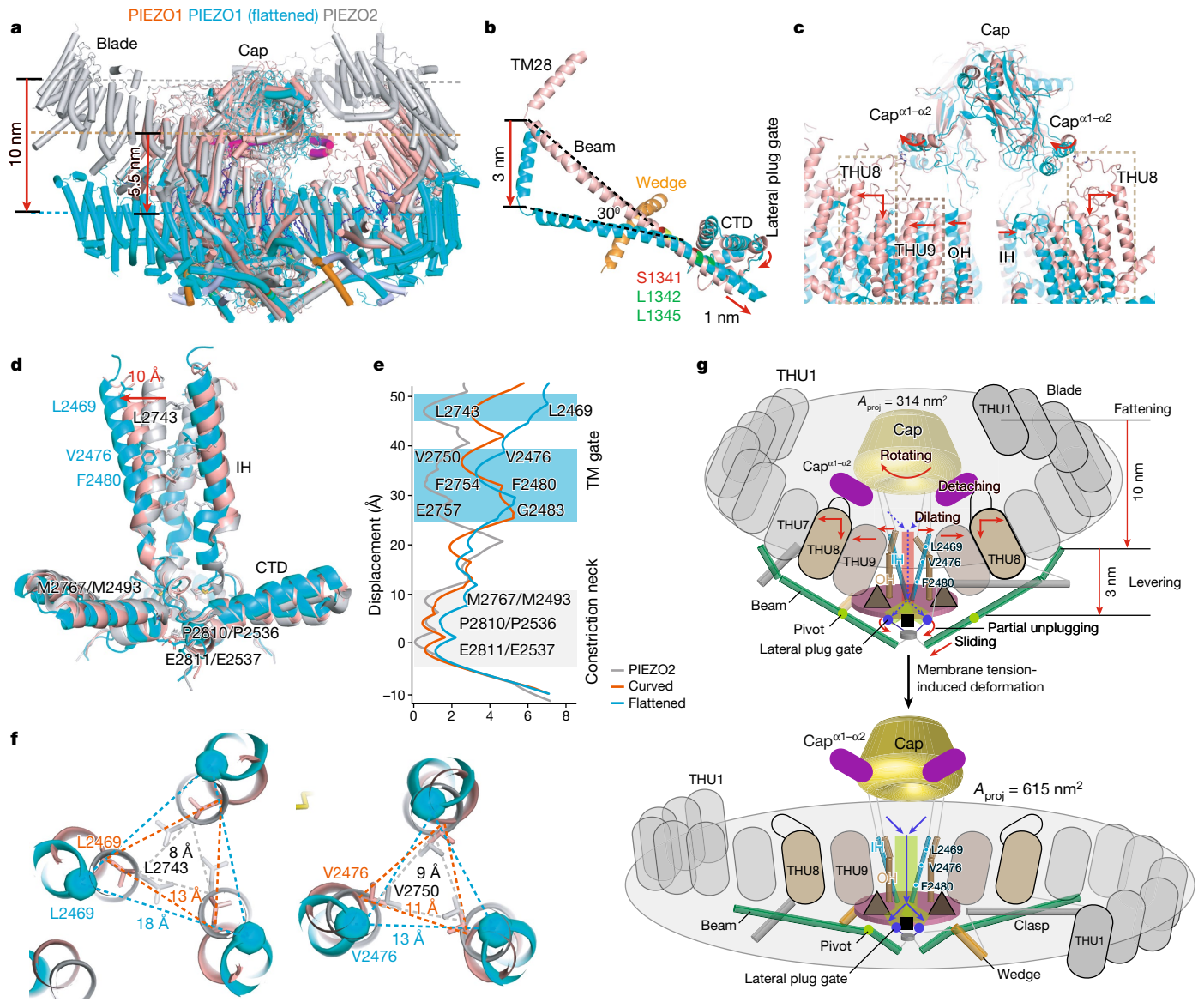


Fig. 4 | Structural rearrangement from the curved to the flattened structures. **a**, Side view of the superimposed curved and flattened PIEZO1 structures and the PIEZO2 structure (PDB ID: 6KG7). Dashed lines indicate the middle plane of the most distal blade of PIEZO2 (grey), THU4 of the curved PIEZO1 (salmon) and THU4 of the flattened PIEZO1 (cyan). The downward displacement of the distal blade of PIEZO2 and the THU4 of the curved PIEZO1 to the fully flattened PIEZO1 are labelled. **b**, The superimposed beam of the curved and flattened PIEZO1 structures showing the lever-like motion at S1341 and the proposed pivot residues L1342 and L1345. **c**, The superimposed curved and flattened structures of PIEZO1 showing the detachment of the cap from the extracellular loop of THU8 and displacement of the THU9, outer helix (OH) and inner helix (IH). **d**, Side view of the superimposed inner helices and C-terminal

domains of the curved and flattened PIEZO1 structures (salmon red and cyan, respectively) and PIEZO2 (grey). **e**, Pore radius along the central axis of the ion conduction pathway of the indicated PIEZO2, and the curved and flattened structures of PIEZO1 from proteoliposomes. The pore radius of the flattened structure is presumptive as it lacks precise side-chain density. The residues forming the transmembrane helix gate and intracellular constriction neck are labelled. **f**, Superimposed inner helices of the curved and flattened PIEZO1 structures (salmon red and cyan, respectively) and PIEZO2 (grey) zoomed in at the indicated transmembrane gate residues. The distance between the specified residues located in neighbouring inner helices is shown. **g**, Schematic of the structural rearrangement upon transition from the curved to the flattened state. Two of the three subunits are illustrated for clarity.

2 nm on the membrane plane (Extended Data Fig. 8a, Supplementary Video 1), consistent with an in-plane area expansion. The blade domain undergoes a vertical downward movement to become completely co-planar (Fig. 4a, Supplementary Video 2). On the basis of the full PIEZO2 structure and the estimated 10-nm height of the blade of the curved PIEZO1 in proteoliposomes, the most distal blade is expected to show a downward movement of about 10 nm when transitioned from the curved to the flattened state (Fig. 4a). Flattening of the blade

leads to a sliding of the intracellular beam approximately 1 nm toward the centre (Fig. 4b, Supplementary Video 2), allowing the previously proposed pivot residues L1342 and L1345 to be positioned underneath the C-terminal domain triangular plane⁸ (Fig. 4b). A kinking motion then occurred S1341, immediately before the pivot position, resulting in a 3-nm downward movement of the distal beam (Fig. 4b). This lever-like motion supports the proposal that the intracellular beam functions as a lever to convert large conformational changes of the peripheral blade

into a smaller motion of the central region^{8,30,31}. The collective motion of the beam would cause conformational changes of the following central plug, lateral plug and wedge domains (Fig. 4b, Extended Data Fig. 1a). In the flattened structure, the density for the unmodelled central plug become less apparent compared with the curved map (Extended Data Fig. 6f) and the wedge domain appears (Fig. 4b). Previous studies have proposed that the lateral plug may undergo partial unplugging upon channel opening³². Therefore, such conformational changes may be too dynamic to be resolved at the current medium-resolution map of the flattened structure. In line with this possibility, 3D classification reveals that in one class of the 3D maps, the density corresponding to the lateral plug becomes fragmented (Extended Data Fig. 6g). Collectively, these structural analyses suggest that flattening the distal blade and levering the beam lead to gating of the intracellular lateral plug gate (Fig. 4g).

Detach the cap to gate the central pore

In the curved state, the extracellular loop of THU8 interacts with the α 1-helical domain of the cap involving electrostatic interactions¹⁰ (Figs. 2c, 4c). Deleting the whole cap domain or the α 1- and α 2-helical domains of the cap, or specifically crosslinking the cap α 1-helix with the extracellular loop of THU8 abolished mechanical activation of PIEZO1³³, consistent with a critical role of the cap in gating the transmembrane pore. Flattening the blade leads to a downward and tilting movement of the THU8 and its extracellular loop, resulting in a full detachment of the cap from the blade (Figs. 2g, 4c). The clockwise rotation of the detached cap and outward shift of the THU9 may collectively cause the expansion of the outer portion of the outer helix and the pore-lining inner helix (Fig. 4c–e, Extended Data Fig. 8b, c, Supplementary Video 3). Previous studies have proposed the existence of a hydrophobic gate defined by the upper residue L2469 and the lower residues V2476 and F2480 in PIEZO1 (the corresponding residues in PIEZO2 are L2743, V2750 and F2754) (Fig. 4d–f), which could be gated by motion of the top cap domain⁷. In line with this, the cap domain displays a continuous clockwise rotation from PIEZO2 to the curved and flattened PIEZO1 (Extended Data Fig. 8c). Comparison of both the overall pore-radius profile (this is presumptive for the flattened structure, owing to the lack of precise side-chain density) (Fig. 4e) and the main-chain distance of the gating residues (Fig. 4f) shows a more dilated transmembrane pore in the flattened structure than those of the curved PIEZO1 and PIEZO2 structures. For instance, the distance of the main chain positions of L2469 in neighbouring inner helices is increased from 13 Å in the curved state to 18 Å in the flattened state and that of V2476 was increased from 11 Å to 13 Å (Fig. 4f). The distances of the corresponding gate residues L2743 and V2750 in PIEZO2 were 8 Å and 9 Å, respectively (Fig. 4f). Given the approximately 10 Å dilation of the gating residue L2469 from the fully closed pore of PIEZO2 to the flattened state of PIEZO1 (Fig. 4d–f), the flattened structure may represent an open transmembrane pore. Nevertheless, we could not exclude the possibility that the flattened structure represents an inactive state. In line with this scenario, the modestly dilated V2476 has previously been proposed to form an inactivation gate³⁴. Regardless of the exact functional state of the flattened structure, the dynamic decoupling of the cap and the blade may result in gating of the central transmembrane pore (Fig. 4g).

The transmembrane pore is followed vertically by the intracellular constriction neck (Fig. 4d, e). However, we did not observe major structural changes of the constricting residues including M2493, P2536 and E2537 in the transition from the curved to the flattened structures (Fig. 4d, e, Extended Data Fig. 8d). Together with previous functional characterizations³², these structural analyses suggest that the intracellular constriction neck does not form a dynamic gate to allow ion conduction. Notably, both the curved and flattened structures contain the pore lipid (Extended Data Figs. 5c, d, 8b). Molecular dynamics simulations

of PIEZO1 have indicated the movement of lipids in the pore region³⁵. Thus, the pore lipid may potentially contribute to the gating of PIEZO1.

Concluding remarks

The curved and flattened structures of PIEZO1 in liposomes (Figs. 1, 2) provide a paradigm for determining and analysing structural dynamics of ion channels in lipid bilayers and represent a major technical advance in structural and mechanistic studies of ion channels in general. Mechanistically, our studies have provided a fundamental understanding of how PIEZO1 uses its intrinsic deformability and structural rearrangement to simultaneously achieve its extraordinary mechanosensitivity for channel gating and selective cation permeation. First, the curved and flattened structures of PIEZO1 conform to the droplet-shaped and D-shaped liposome vesicles (Figs. 1, 2), providing conclusive evidence that PIEZO1 can both curve the lipid membranes and respond directly to the changes in membrane tension associated with changes in membrane curvature. Second, the PIEZO1–membrane system undergoes an in-plane membrane areal expansion of about 300 nm² during the transition from the curved to the flattened state (Fig. 3), which is equivalent in magnitude to the change in lateral membrane tension and the difference in free energy required to convert the channel from the closed to the open state. Combining the previously determined equation describing the force-induced displacement of the blade¹¹, we calculate that a transition from the curved to the flattened state requires a mechanical force of approximately 92 nN, work of approximately 570 pN nm and a half-maximal tension of 1.9 pN nm⁻¹ (Fig. 3c), close to the experimentally measured T_{50} value for PIEZO1 activation³ of 1.4 pN nm⁻¹. Thus, we have established a precise and quantitative description of the intrinsically curvature-based mechanosensitivity of PIEZO1. Third, although the moderate resolution of ion-conducting pathway in the flattened structure does not permit a conclusive assignment of its functional state, we observe that the marked deformation of the mechanosensing blade is converted to a modest change in the transmembrane gate and the lateral plug gate through the motion of the extracellular cap and the intracellular beam, respectively (Fig. 4g), ensuring the simultaneous high mechanosensitivity and cation selectivity.

Online content

Any methods, additional references, Nature Research reporting summaries, source data, extended data, supplementary information, acknowledgements, peer review information; details of author contributions and competing interests; and statements of data and code availability are available at <https://doi.org/10.1038/s41586-022-04574-8>.

- Coste, B. et al. Piezo1 and Piezo2 are essential components of distinct mechanically activated cation channels. *Science* **330**, 55–60 (2010).
- Coste, B. et al. Piezo proteins are pore-forming subunits of mechanically activated channels. *Nature* **483**, 176–181 (2012).
- Lewis, A. H. & Grandl, J. Mechanical sensitivity of Piezo1 ion channels can be tuned by cellular membrane tension. *eLife* **4**, e12088 (2015).
- Xiao, B. Levering mechanically activated Piezo channels for potential pharmacological intervention. *Annu. Rev. Pharmacol. Toxicol.* **60**, 195–218 (2020).
- Kefauver, J. M., Ward, A. B. & Patapoutian, A. Discoveries in structure and physiology of mechanically activated ion channels. *Nature* **587**, 567–576 (2020).
- Ge, J. et al. Architecture of the mammalian mechanosensitive Piezo1 channel. *Nature* **527**, 64–69 (2015).
- Wang, L. et al. Structure and mechanogating of the mammalian tactile channel PIEZO2. *Nature* **573**, 225–229 (2019).
- Zhao, Q. et al. Structure and mechanogating mechanism of the Piezo1 channel. *Nature* **554**, 487–492 (2018).
- Saotome, K. et al. Structure of the mechanically activated ion channel Piezo1. *Nature* **554**, 481–486 (2018).
- Guo, Y. R. & MacKinnon, R. Structure-based membrane dome mechanism for Piezo mechanosensitivity. *eLife* **6**, e33660 (2017).
- Lin, Y. C. et al. Force-induced conformational changes in PIEZO1. *Nature* **573**, 230–234 (2019).
- Jiang, Y., Yang, X., Jiang, J. & Xiao, B. Structural designs and mechanogating mechanisms of the mechanosensitive piezo channels. *Trends Biochem. Sci.* **46**, 472–488 (2021).

13. Li, J. et al. Piezo1 integration of vascular architecture with physiological force. *Nature* **515**, 279–282 (2014).
14. Ranade, S. S. et al. Piezo1, a mechanically activated ion channel, is required for vascular development in mice. *Proc. Natl Acad. Sci. USA* **111**, 10347–10352 (2014).
15. Jiang, F. et al. The mechanosensitive Piezo1 channel mediates heart mechano-chemo transduction. *Nat. Commun.* **12**, 869 (2021).
16. Wang, S. et al. Endothelial cation channel PIEZO1 controls blood pressure by mediating flow-induced ATP release. *J. Clin. Invest.* **26**, 4527–4536 (2016).
17. Rode, B. et al. Piezo1 channels sense whole body physical activity to reset cardiovascular homeostasis and enhance performance. *Nat. Commun.* **8**, 350 (2017).
18. Sun, W. et al. The mechanosensitive Piezo1 channel is required for bone formation. *eLife* **8**, e47454 (2019).
19. Cahalan, S. M. et al. Piezo1 links mechanical forces to red blood cell volume. *eLife* **4**, e07370 (2015).
20. Solis, A. G. et al. Mechanosensation of cyclical force by PIEZO1 is essential for innate immunity. *Nature* **573**, 69–74 (2019).
21. Marshall, K. L. et al. PIEZO2 in sensory neurons and urothelial cells coordinates urination. *Nature* **588**, 290–295 (2020).
22. Nonomura, K. et al. Piezo2 senses airway stretch and mediates lung inflation-induced apnoea. *Nature* **541**, 176–181 (2017).
23. Ranade, S. S. et al. Piezo2 is the major transducer of mechanical forces for touch sensation in mice. *Nature* **516**, 121–125 (2014).
24. Woo, S. H. et al. Piezo2 is the principal mechanotransduction channel for proprioception. *Nat. Neurosci.* **18**, 1756–1762 (2015).
25. Woo, S. H. et al. Piezo2 is required for Merkel-cell mechanotransduction. *Nature* **509**, 622–626 (2014).
26. Zeng, W. Z. et al. PIEZOs mediate neuronal sensing of blood pressure and the baroreceptor reflex. *Science* **362**, 464–467 (2018).
27. Chesler, A. T. et al. The role of PIEZO2 in human mechanosensation. *New Engl. J. Med.* **375**, 1355–1364 (2016).
28. Szczot, M. et al. PIEZO2 mediates injury-induced tactile pain in mice and humans. *Sci. Transl. Med.* **10**, eaat9892 (2018).
29. Jumper, J. et al. Highly accurate protein structure prediction with AlphaFold. *Nature* **596**, 583–589 (2021).
30. Wang, Y. et al. A lever-like transduction pathway for long-distance chemical- and mechano-gating of the mechanosensitive Piezo1 channel. *Nat. Commun.* **9**, 1300 (2018).
31. Zhao, Q., Zhou, H., Li, X. & Xiao, B. The mechanosensitive Piezo1 channel: a three-bladed propeller-like structure and a lever-like mechanogating mechanism. *FEBS J.* **286**, 2461–2470 (2018).
32. Geng, J. et al. A plug-and-latch mechanism for gating the mechanosensitive Piezo channel. *Neuron* **106**, 438–451.e436 (2020).
33. Lewis, A. H. & Grandl, J. Inactivation kinetics and mechanical gating of Piezo1 ion channels depend on subdomains within the cap. *Cell Rep.* **30**, 870–880.e872 (2020).
34. Zheng, W., Gracheva, E. O. & Bagriantsev, S. N. A hydrophobic gate in the inner pore helix is the major determinant of inactivation in mechanosensitive Piezo channels. *eLife* **8**, e44003 (2019).
35. De Vecchis, D., Beech, D. J. & Kalli, A. C. Molecular dynamics simulations of Piezo1 channel opening by increases in membrane tension. *Biophys. J.* **120**, 1510–1521 (2021).

Publisher's note Springer Nature remains neutral with regard to jurisdictional claims in published maps and institutional affiliations.

© The Author(s), under exclusive licence to Springer Nature Limited 2022, corrected publication 2022

Methods

Expression and purification of mouse PIEZO1 proteins

The purification procedure was similar to the previously described protocol except for the change of detergent C₁₂E₉ to C₁₂E₁₀ in the cell lysis buffer⁸. In brief, 36 h after transfection with the PIEZO1-pp-GST-IRES-GFP expression vector that expresses the PIEZO1–glutathione S-transferase (GST) fusion protein with a precision protease cleavage site in between, HEK 293T Cells (from ATCC) were collected and homogenized by lysis buffer, containing 25 mM Na-PIPES, pH 7.2, 150 mM NaCl, 1% (wt/vol) detergents CHAPS, 0.1% C₁₂E₁₀, 0.5% L- α -phosphatidylcholine (Avanti) and a cocktail of protease inhibitors (Roche) for 1 h. After centrifugation at 100,000g for 30 min, the supernatant was collected and incubated with glutathione–sepharose beads at 4 °C for 6 h. The Piezo1 protein was freed from the resin by the cleavage of 0.1 mg ml⁻¹ PreScission Protease, and processed to the size-exclusion chromatography (SEC) (Superpose-6 10/300 GL increase, GE Healthcare) in the buffer containing 25 mM Na-PIPES, pH 7.2, 150 mM NaCl and 0.026% C₁₂E₁₀. Peak fractions between 11.5 ml and 13 ml containing well-dispersed trimeric PIEZO1 proteins (Extended Data Fig. 1b, c) were collected for further reconstitution assays.

Reconstitution of PIEZO1 proteoliposomes

Given the approximately 0.9-MDa size and 114 transmembrane helices of the PIEZO1 channel, we explored experimental conditions to achieve efficient proteoliposome reconstitution and homogenous size of the liposome vesicles suitable for single-particle cryo-EM structure determination. The workflow for reconstitution of the purified PIEZO1 proteins was illustrated in Fig. 1a. Detergent-solubilized liposomes were mixed with purified PIEZO1 proteins. Once detergents were removed, the transmembrane region of PIEZO1 proteins tended to insert into the liposomes to form proteoliposomes. To prepare liposomes, L- α -phosphatidylcholine, 20% (soy) (Soy Total Lipid Extract) (Avanti) was dissolved in chloroform and dried in a rotary vacuum evaporator at 38 °C water bath for 6 h to eliminate any residual chloroform. The lipid film was resuspended in the reconstitution buffer A (25 mM Na-PIPES, pH 7.2, 150 mM NaCl) to reach a lipid concentration at 40 mg ml⁻¹. After a 10-min sonication, the lipid solution underwent 8 freeze–thaw cycles (liquid nitrogen–water bath at 40 °C) to reduce multilamellar vesicles, followed by repetitive extrusion (31 times) through Nuclepore filters (100 nm pore size) using an Avanti Mini-Extruder to obtain liposomes around 100 nm. The liposome solution was further solubilized by 2% detergents and then mix with purified PIEZO1 proteins to get a protein/lipid ratio at 1:4 (wt:wt). Bio-Beads SM-2 adsorbent (Bio-RAID) was first tried to remove the detergent. For 100 μ l reconstitution solution, 80 mg beads were added at half an hour interval (10 mg each time) and rotated overnight to ensure all the detergents were absorbed. This method did not result in efficient reconstitution, exemplified by the large empty liposomes (>100 nm) and PIEZO1 protein aggregates (Extended Data Fig. 1d). We then tried dialysis for detergent removal. One-hundred microlitres reconstitution solution was dialysed against 1 l buffer A for 3 days with daily buffer change. However, we found that detergent micelles (especially for those detergents with low critical micelle concentration (CMC)) could not be totally cleaned up, resulting in fragmented liposomes (Extended Data Fig. 1e). Therefore, we switched to the detergent decyl maltoside (DM) with a high CMC at 1.8 mM for lipid solubilization and adopted SEC for detergent removal (Extended Data Fig. 1f). This strategy had been successfully applied to human BK channels³⁶ and *Escherichia coli* AcrB transporter proteoliposome reconstitutions³⁷. Liposomes made from 3.2 mg soy lipid were solubilized by 2% decyl maltoside at room temperature and incubated with 0.8 mg PIEZO1 proteins at 4 °C. One hour later, the protein–lipid–detergent mixture was loaded into a gravity column packed with 18 ml Sephadex G-50 resin (superfine, Sigma-Aldrich), and the reconstituted proteoliposomes were contained in the fractions between 4.5–7.0 ml.

In summary, after testing various detergent and lipid compositions and detergent removal methods (Extended Data Fig. 1d–f), we have eventually found that using decyl maltoside-solubilized soybean lipids and SEC for detergent removal resulted in efficient reconstitution of PIEZO1 into well-shaped liposome vesicles of different sizes (Extended Data Fig. 1f).

Density centrifugation of the reconstituted PIEZO1 proteoliposomes

The resulting proteoliposomes were further separated from empty liposomes and free PIEZO1 aggregates through a discontinuous gradient centrifugation process³⁸. The collected sample from Sephadex G-50 column was concentrated to a volume less than 250 μ l (Amicon Ultra centrifugal filter, 4 ml, 100-kDa cut-off), and further separated by a gradient centrifugation. The protocol was adapted from the previously described procedures³⁸ except by substituting Nycodenz with iodixanol medium (Sigma-Aldrich). In brief, a discontinuous gradient was constructed by layering 7 different concentrations of iodixanol (0%, 1%, 3%, 5%, 15%, 20%, 30%; from top to bottom) and the proteoliposome or empty liposome sample was set in the 20% layer at the beginning. After 16 h centrifugation at 50,000g, each layer was collected, stained with Bradford dye (Bio-Rad) and checked via negative-staining electron microscopy. The empty liposomes were mainly floated into the layers of 3–5% exemplified by large burst vesicles under electron microscopy, while the liposomes reconstituted with PIEZO1 stayed in the layers of 15–20% (Extended Data Fig. 1g). For further cryo-sample preparation, the 20% layer was collected and the iodixanol was removed by 7 repetitive dilution–concentration cycles (1:5 dilution) and then concentrated by a Amicon Ultra centrifugal filter (0.5 ml, 100-kDa cut-off) to a minimal volume (about 12 μ l). The resulting sample was just enough for preparing one cryo-sample on a holey Quantifoil Au grid. For a graphene grid, the proteoliposome sample was diluted in a 1:10 ratio.

Negative-stain electron microscopy

Four microlitres of freshly prepared sample was loaded to a glow-discharged (PELCO) carbon-coated copper grid (300 mesh, Zhongjingkeyi Technology) and incubated for 1 min. The excess sample liquid was removed with a filter paper and then 4 μ l buffer was applied to the grid to wash the carbon surface³⁸. After 15 s, the excess buffer was removed with filter paper, and then the grid was stained with a droplet of 2% uranyl acetate for 20 s. The staining process was repeated twice and the third staining process was carried out additionally 30 s. Finally, the excess staining buffer was removed, and the grid was dried at room temperature. The prepared grids were observed on a T12 microscope (FEI) operating at 120 kV, using a 4k \times 4k CCD camera (UltraScan, Gatan) at a nominal magnification of 49,000 with a calibrated pixel size of 2.3 Å.

Electron microscopy sample preparation and image collection

We optimized cryo-preparation of PIEZO1 proteoliposomes to obtain high-quality cryo-samples with well-distributed particles because hydrophobic liposomes tend to stick on the supporting carbon film area instead of penetrating into the hole area (Extended Data Fig. 1h). Indeed, cryo-electron tomography imaging revealed that the majority of PIEZO1 proteoliposomes stayed in the air–water interface (Extended Data Fig. 1i). After trials, we have found that a combination of prolonged glow discharge treatment to 40 s and multi-application of the proteoliposome sample resulted in evenly distributed cryo-samples in the Quantifoil grid (Fig. 1b and Extended Data Fig. 1j). Furthermore, consistent with the previous report³⁷, the addition of a super-thin layer of hydrophobic graphene on the grid would further facilitate the penetration of proteoliposomes at a much lower concentration (Extended Data Fig. 2a).

The cryo-samples were prepared in a Vitrobot Mark IV (Thermo Fisher) with a chamber temperature of 8 °C with 100% humidity. For Quantifoil Au grids (Holey gold, R1.2/1.3, 200mesh), the long-time

incubation method and the multi-application method were combined^{39,40}. In brief, the grids were pre-treated with the glow discharge for 40 s or the specifically indicated time, and then 4 μ l freshly prepared PIEZO1 proteoliposome or liposome sample was mixed with 0.65 mM fluorinated fos-choline-8 (Hampton) and loaded onto the grid. After a 2-min incubation, the excess liquid was removed from the grid. The load-incubation-removal process was repeated twice before blotting for 5.5 s with a nominal blot force 0 of the Vitrobot and then, the grid was immediately plunged into pre-cooled liquid ethane for vitrification. For graphene grids (gifts from the H. Wang laboratory), a drop of sample was loaded onto the glow discharged grid and stayed for 1 min, and then blotted for 4 s before being plunge frozen.

The prepared grids were observed using a 300 kV Titan Krios (FEI) electron microscope equipped with a Cs corrector and GIF Quantum energy filter (slit width 20 eV). Micrographs were recorded with a K3 Summit direct electron detector (Gatan) working at the super-resolution mode. Data acquisition was performed using AutoEMation⁴¹ under a nominal magnification of 64,000 yielding a super-resolution pixel size of 0.549 Å, and a defocus range from -1.5 to -2.4 μm. The total exposure time was set to 2.56 s with 0.08 s per frame yielding a 32-frame stack. The total dose was approximately 50 e⁻ Å⁻² for each micrograph.

Image processing

Simplified schemes of the procedure for image processing are presented in Extended Data Figs. 4, 7. A total of 35,314 and 16,389 cryo-EM micrographs were collected from the samples using Quantifoil grids and graphene grids, respectively. The flattened structure of PIEZO1 was derived from the sample using the Quantifoil grids, while the curved state was mostly derived from the samples on the graphene girds and partially from samples on the Quantifoil grids. All the micrographs were motion-corrected using the MotionCor2 program⁴² with a 11 × 11 patch and a two-fold binning, resulting in a pixel size of 1.098 Å. Contrast transfer function (CTF) parameters were estimated by CTFFIND4.1 with exhaustive searching⁴³. The particle picking was performed by Relion3.1⁴⁴ and EPicker (homemade, unpublished, <http://thuem.net>). First, about 1,000 particles were manually picked and used to generate PIEZO1 templates (by 2D classification) for further particle picking of the PIEZO1 complexes in the flattened state by Relion. Then, the liposomes were picked by EPicker and subjected to 2D classification to locate PIEZO1 particles in the curved state. For all the picked particles, visually good ones were further selected and re-centred to the PIEZO1 complexes by analyzing the image alignment results from 2D classification through THUNDER⁴⁵. After particle extraction based on the centred particle coordinates, further 2D classification and deep 2D classification³⁷ were performed to remove bad particles. Finally, 119,956 and 777,773 particles in flattened state and the curved state, respectively, were selected for the further 3D analysis by THUNDER (Extended Data Figs. 4, 7).

The 3D analysis was performed by THUNDER. The sub-dataset of the PIEZO1 in the curved state was processed as the following. A PIEZO1 map (EMD-6865) was low-pass filtered to 45 Å and used as the initial model. The parameter “Ignore Signal Under” was set to 120 Å to reduce the influence of the low frequency signal in alignment. Then, a map reported at 17 Å resolution was calculated and revealed the cap domain and the bottom of beam and transmembrane gate domain. Then, multiple 3D classifications with 6 classes were carried out. The best classes achieved 12 Å resolution indicated by the presence of five THUs near the central channel. Most classes showed correct PIEZO1 features and presented continuously changed conformation of PIEZO1 complexes. To improve the resolution, further 3D classification was performed using 3 reference maps selected from the previous 3D classifications. One of the reference maps was derived from liposomes without the embedded PIEZO1, while the other two were derived from liposomes with reconstructed PIEZO1, but displayed two most distinct

conformational states of PIEZO1. Some 635,097 particles were selected and the resolution was pushed to 8 Å. Then, more rounds of local 3D classifications were performed to further remove the bad particles. In each 3D classification, those classes with poor PIEZO1 density were removed, and the best class was used as the initial model of next round. Finally, 209,166 particles remained and the resolution was pushed to 3.95 Å. These particles were subjected to 3D refinement with a tight mask. The final resolution of the map was 3.46 Å. The data processing for the PIEZO1 complexes in the flattened state was similar to that in the curved state, but only 35,012 particles were retained to produce a map with an overall resolution of 6.81 Å, but the local resolution of the transmembrane region reaching about 4.8 Å, allowing 26 transmembrane helices clearly resolved. All the 3D refinement and 3D classification were performed with C3 symmetry. The reported resolutions were based on the gold-standard Fourier shell correlation at 0.143 criterions. Variations in local resolution were estimated using Resmap⁴⁶.

Cryo-electron tomography data collection and reconstruction

The solution containing the freshly reconstituted PIEZO1 liposomes was added with 0.65 mM FFC-8 and frozen on glow-discharged Quantifoil 200 mesh gold 1.2/1.3 grids. The samples were observed using the 300 kV Titan Krios electron microscope. Micrographs were recorded in super-resolution mode at a nominal magnification of 64,000, resulting in a calibrated pixel size of 0.549 Å. Tilt-series were collected using the bidirectional tilt scheme, first from 15 to -60° and followed from 15° to 60° with a 3° step, at defocus ranging from -4 to -6 μm by SerialEM⁴⁷. At each tilt angle, micrograph with 8 frames (0.213 s per frame) was recorded. The total dose for a tilt series is 123 e⁻ Å⁻². Beam induced motion were corrected using MotionCor2. Tilt series were aligned and reconstructed to tomograms in IMOD⁴⁸. The segmentation of the PIEZO1-proteoliposome was performed with EMAN⁴⁹.

Model building and structure refinement

For the PIEZO1 structure in the curved state, the previously determined cryo-EM structures of PIEZO1 (PDB: 5Z10 and 6B3R) were aligned to the cryo-EM map by Chimera⁵⁰, and used as the initial models. Manual fitting was performed using COOT⁵¹. Then the model was refined in real space using PHENIX with secondary structure and non-crystallographic symmetry (NCS) restraints. Lipid-like densities appeared in the density maps were fitted by trial with candidate lipids. For the PIEZO1 structure in the flattened state, the PIEZO1 model in the curved state was used as the starting point, and was split into several parts to be fitted into the map in the flattened state by Chimera. The rest process of model building was similar to the curved state. In addition, compared to the curved state, the extra density in the map of the flattened state was recognized and the model was built according to the prediction by AlphaFold2²⁹. The final atomic model was validated using MolProbity⁵².

Measurement of the curvature induced by PIEZO1 embedded in proteoliposome

To measure the curvature variance induced by the reconstituted PIEZO1 in proteoliposome vesicles, the Canny edge detection method was first used to detect the inner and outer edge of the proteoliposome vesicles. After removing the mis-detected edges, the Hough transform was performed on the detected edge arcs at either the side with the residing PIEZO1 or the opposite pole of the same vesicle, leading to the measurement of the R_{PIEZO1} and R_{liposome} , respectively. Canny edge detection and Hough transform were calculated using the library OpenCV.

Statistics and reproducibility

PIEZO1 proteins were successfully purified and reconstituted into liposomes more than ten times. Figure 1b and Extended Data Fig. 2a, b were representative micrographs of at least three independent data collections with similar results. During the optimization of PIEZO1 reconstitution and cryo-sample preparation, each condition was

Article

independently tested twice with similar outcomes, and Extended Data Fig. 1c–h,j presents representative micrographs.

Reporting summary

Further information on research design is available in the Nature Research Reporting Summary linked to this paper.

Data availability

The coordinates of the curved and flattened PIEZO1 structures derived from proteoliposomes were deposited in the Protein Data Bank under accessions 7WLT and 7WLU, respectively. The corresponding cryo-EM maps were deposited in the Electron Microscopy Data Bank (EMDB) under accessions EMD-32592 and EMD-32593, respectively.

36. Wang, L. & Sigworth, F. J. Structure of the BK potassium channel in a lipid membrane from electron cryomicroscopy. *Nature* **461**, 292–295 (2009).
37. Yao, X., Fan, X. & Yan, N. Cryo-EM analysis of a membrane protein embedded in the liposome. *Proc. Natl. Acad. Sci. USA* **117**, 18497–18503 (2020).
38. Baxa, U. Imaging of liposomes by transmission electron microscopy. *Methods Mol. Biol.* **1682**, 73–88 (2018).
39. Snijder, J. et al. Vitrification after multiple rounds of sample application and blotting improves particle density on cryo-electron microscopy grids. *J. Struct. Biol.* **198**, 38–42 (2017).
40. Tonggu, L. & Wang, L. Cryo-EM sample preparation method for extremely low concentration liposomes. *Ultramicroscopy* **208**, 112849 (2020).
41. Lei, J. & Frank, J. Automated acquisition of cryo-electron micrographs for single particle reconstruction on an FEI Tecnai electron microscope. *J. Struct. Biol.* **150**, 69–80 (2005).
42. Zheng, S. Q. et al. MotionCor2: anisotropic correction of beam-induced motion for improved cryo-electron microscopy. *Nat. Methods* **14**, 331–332 (2017).
43. Rohou, A. & Grigorieff, N. CTFFIND4: fast and accurate defocus estimation from electron micrographs. *J. Struct. Biol.* **192**, 216–221 (2015).
44. Zivanov, J. et al. New tools for automated high-resolution cryo-EM structure determination in RELION-3. *eLife* **7**, e42166 (2018).
45. Hu, M. et al. A particle-filter framework for robust cryo-EM 3D reconstruction. *Nat. Methods* **15**, 1083–1089 (2018).
46. Kucukelbir, A., Sigworth, F. J. & Tagare, H. D. Quantifying the local resolution of cryo-EM density maps. *Nat. Methods* **11**, 63–65 (2014).
47. Mastronarde, D. N. Automated electron microscope tomography using robust prediction of specimen movements. *J. Struct. Biol.* **152**, 36–51 (2005).
48. Kremer, J. R., Mastronarde, D. N. & McIntosh, J. R. Computer visualization of three-dimensional image data using IMOD. *J. Struct. Biol.* **116**, 71–76 (1996).
49. Chen, M. et al. Convolutional neural networks for automated annotation of cellular cryo-electron tomograms. *Nat. Methods* **14**, 983–985 (2017).
50. Pettersen, E. F. et al. UCSF Chimera—a visualization system for exploratory research and analysis. *J. Comput. Chem.* **25**, 1605–1612 (2004).
51. Emsley, P., Lohkamp, B., Scott, W. G. & Cowtan, K. Features and development of Coot. *Acta Crystallogr. D* **66**, 486–501 (2010).
52. Chen, V. B. et al. MolProbity: all-atom structure validation for macromolecular crystallography. *Acta Crystallogr. D* **66**, 12–21 (2010).

Acknowledgements We thank H. Wang, N. Liu and J. Xu for providing the graphene grids; C. Yan for sharing the scripts for deep-2D; L. Wang, H. Zhou, X. Yao, X. Fan, J. Lei and X. Li for technical help; T. Zhao and X. Zhang for developing the Epicker software; the Beijing Frontier Research Center for Biological Structure and Beijing Advanced Innovation Center for Structural Biology for facility and financial support; and the Protein Preparation and Identification Facility at Technology Center for Protein Science in Tsinghua University for facility support. This work was supported by grant numbers 2021ZD0203301, 31825014, 32130049, 32021002, 31630090, 2016YFA0500402 and 2015CB910102 to B.X.; 31570730, 2016YFA0501102 and 2016YFA0501902 to X.L.; from either the Ministry of Science and Technology of the People's Republic of China or the National Natural Science Foundation of China.

Author contributions X.Y. carried out protein purification, proteoliposome reconstitution, cryo-EM sample preparation, data collection, prepared figures and helped with manuscript writing. C.L. performed EM sample preparation, data collection, image processing and model building, and participated in proteoliposome reconstitution. X.C. performed protein purification, proteoliposome reconstitution, cryo-EM sample preparation and data collection. S.L. performed image processing and analysis. X.L. supervised cryo-EM data collection and image processing. B.X. conceived and directed the study, analysed the structure, created figures and wrote the manuscript with help from the other authors.

Competing interests The authors declare no competing interests.

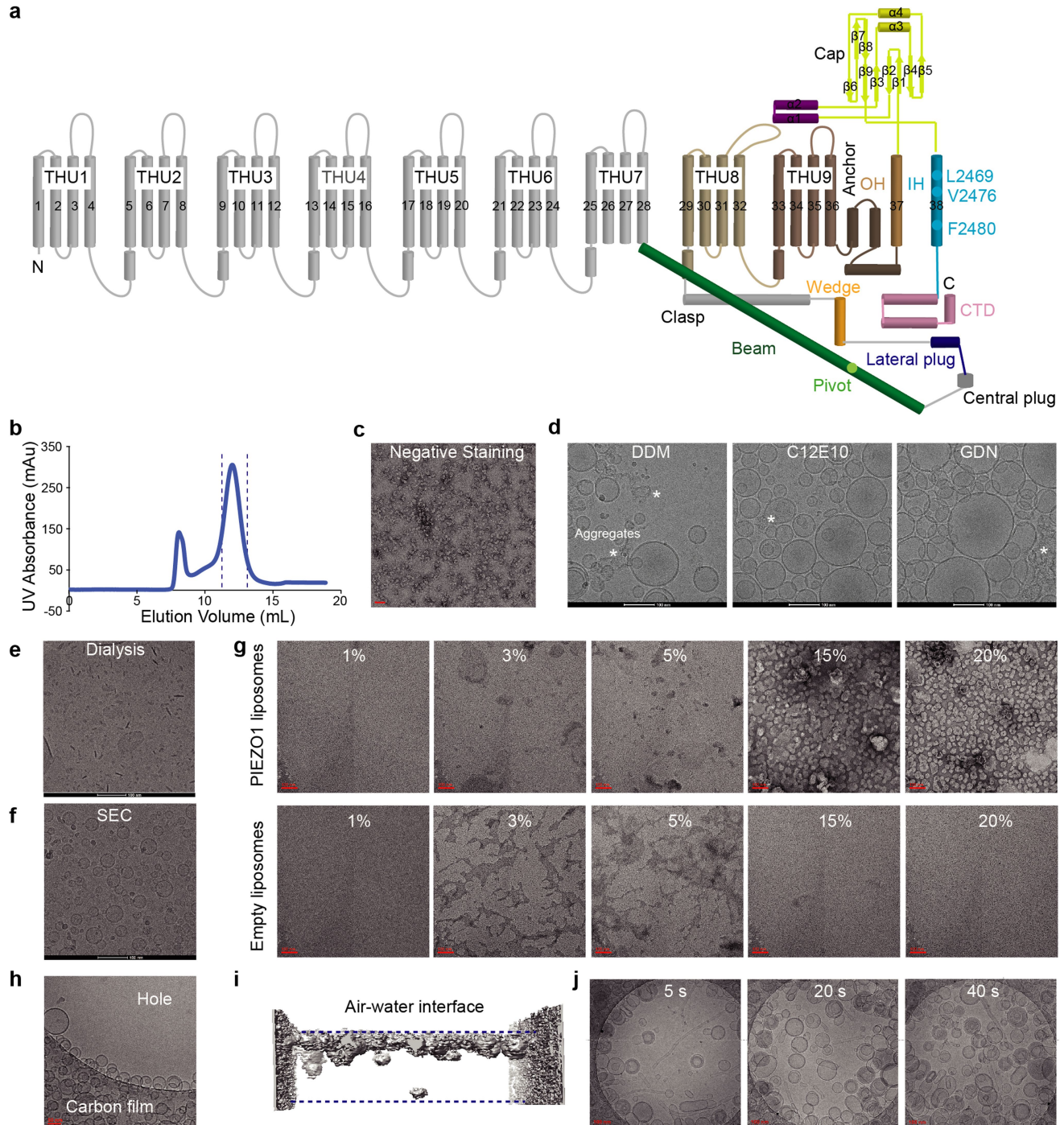
Additional information

Supplementary information The online version contains supplementary material available at <https://doi.org/10.1038/s41586-022-04574-8>.

Correspondence and requests for materials should be addressed to Xueming Li or Bailong Xiao.

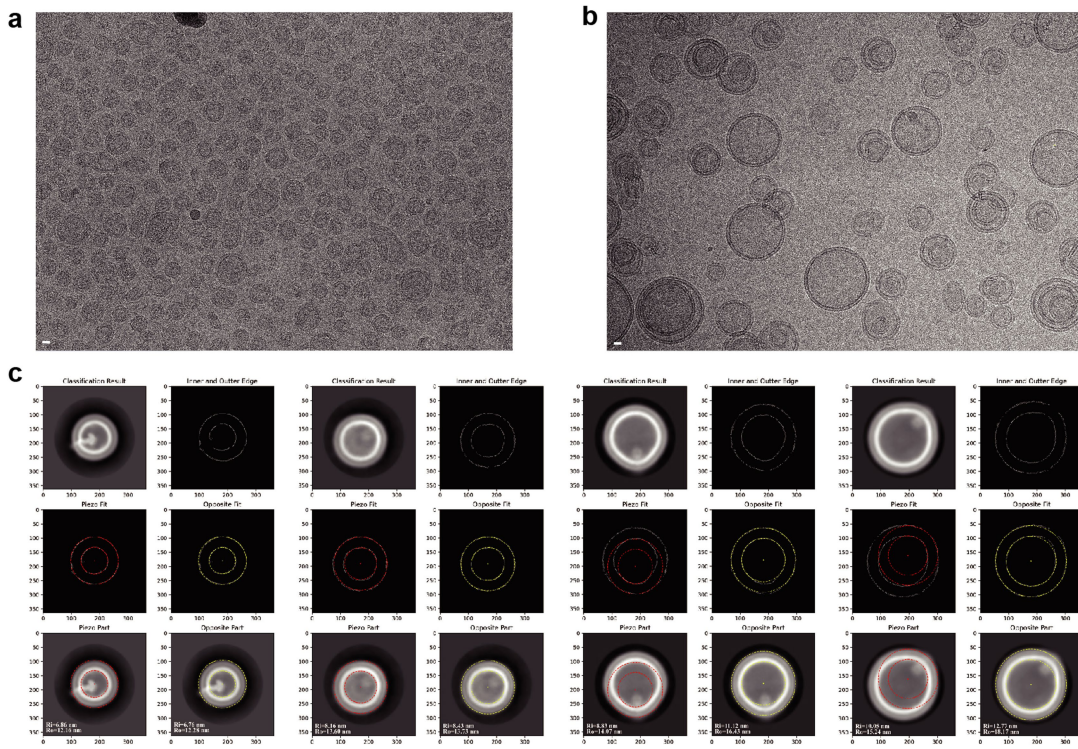
Peer review information *Nature* thanks Yifan Cheng and the other, anonymous, reviewers for their contribution to the peer review of this work. Peer reviewer reports are available.

Reprints and permissions information is available at <http://www.nature.com/reprints>.



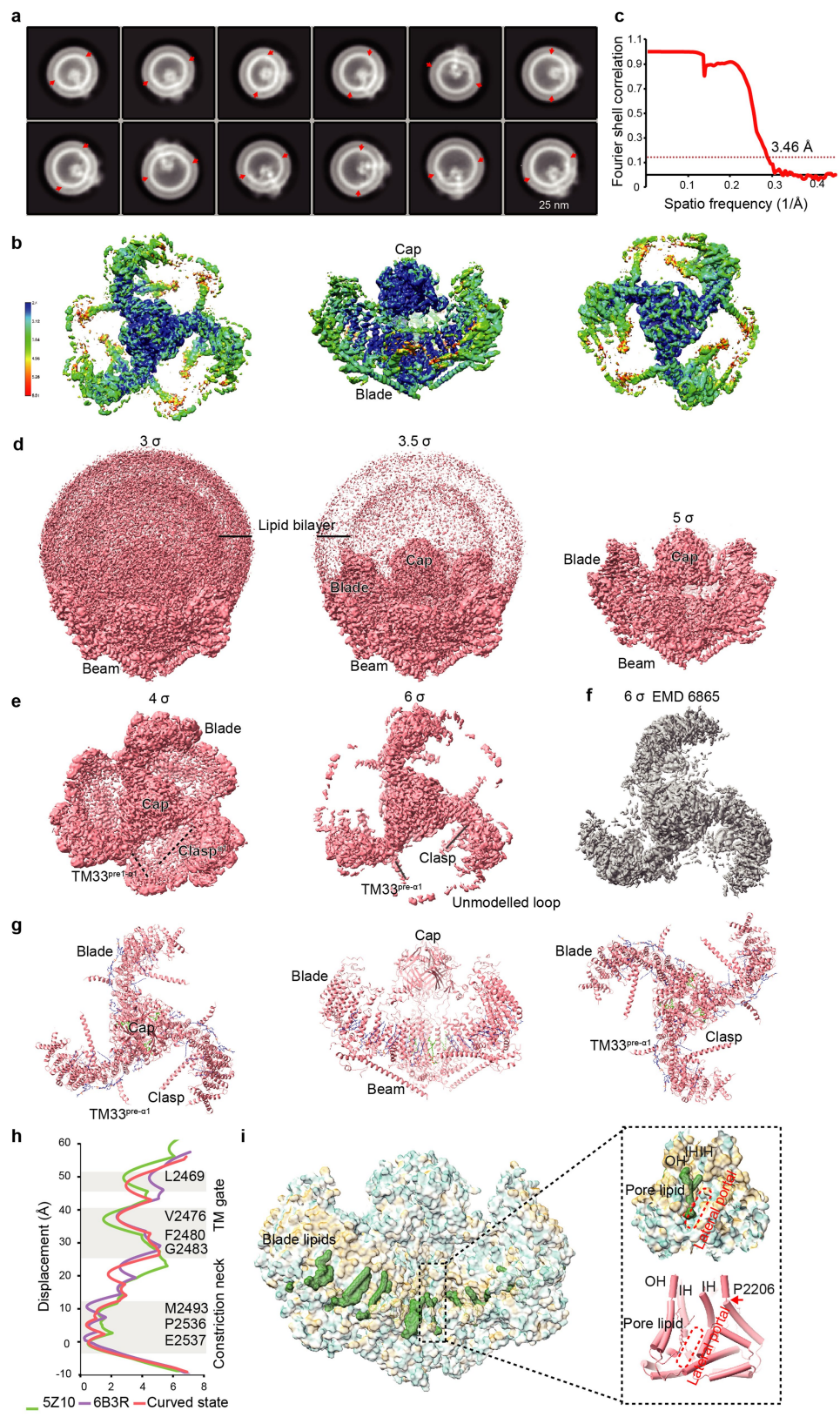
Extended Data Fig. 1 | Optimization of PIEZO1 proteoliposome reconstitution and cryo-EM sample preparation. **a**, The 38-TM topological model of PIEZO1 showing the indicated structural domains. THU: Transmembrane Helical Unit. **b**, A trace of gel filtration of purified PIEZO1 proteins using the detergent C₁₂E₁₀. UV, ultraviolet. Dash lines indicate the peak fractions collected for subsequent studies. **c**, A negative staining EM image of PIEZO1 purified in C₁₂E₁₀. (Scale bar = 50nm). **d**, Cryo-EM images of PIEZO1 proteoliposomes using Bio-beads SM-2 for removing the indicated detergents. The white star indicates the aggregation. **e** and **f**, Cryo-EM images of PIEZO1 proteoliposomes using either dialysis to remove 2% glyco-diosgenin (GDN) (**d**) or SEC for decyl maltoside (DM) removal (**e**). **g**, Negative staining EM images of the indicated fractions after gradient centrifugation. DM solubilized soy lipid were either mixed with PIEZO1 proteins or the same volume of buffer. After

detergent removal, samples were processed into an iodixanol-based gradient centrifugation. **h**, A Cryo-EM image of liposomes sticking on the carbon film. 4 μ L liposome solution was applied to a holey Quantifoil Au grid with a standard 25 s glow discharge pre-treatment. After 30 s incubation, the grid was blotted and plunged into liquid ethane. The image was focused on the border between the hole and carbon film to exhibit the biased liposome distribution. **i**, 3D segmentation of a constructed tomogram showing PIEZO1 proteoliposomes clustered in the air-water interface instead of diffusion into the water. **j**, Distributions of PIEZO1 proteoliposomes on Quantifoil Au grids treated with different glow discharge time. The cryo-samples were prepared by multi-application method described in Method, and prolonged glow-discharge time facilitated the abundant distribution of liposomes in the hole area suitable for cryo-EM imaging.



Extended Data Fig. 2 | Analyses of the deformation of the PIEZO1 proteoliposomes. **a**, Cryo-EM micrograph of PIEZO1 proteoliposomes prepared on the graphene grid (Scale bar = 10nm). **b**, Cryo-EM micrograph of empty liposomes prepared on the Quantifoil Au grid (Scale bar = 10nm). **c**, Analyses of the radii of the PIEZO1-residing side and the opposite pole of the

2D averaged proteoliposomes of varied sizes. The inner and outer bilayers are approximated with the red and yellow dashed circles that are based on the PIEZO1-residing pole and the opposite pole of the same vesicle, respectively.



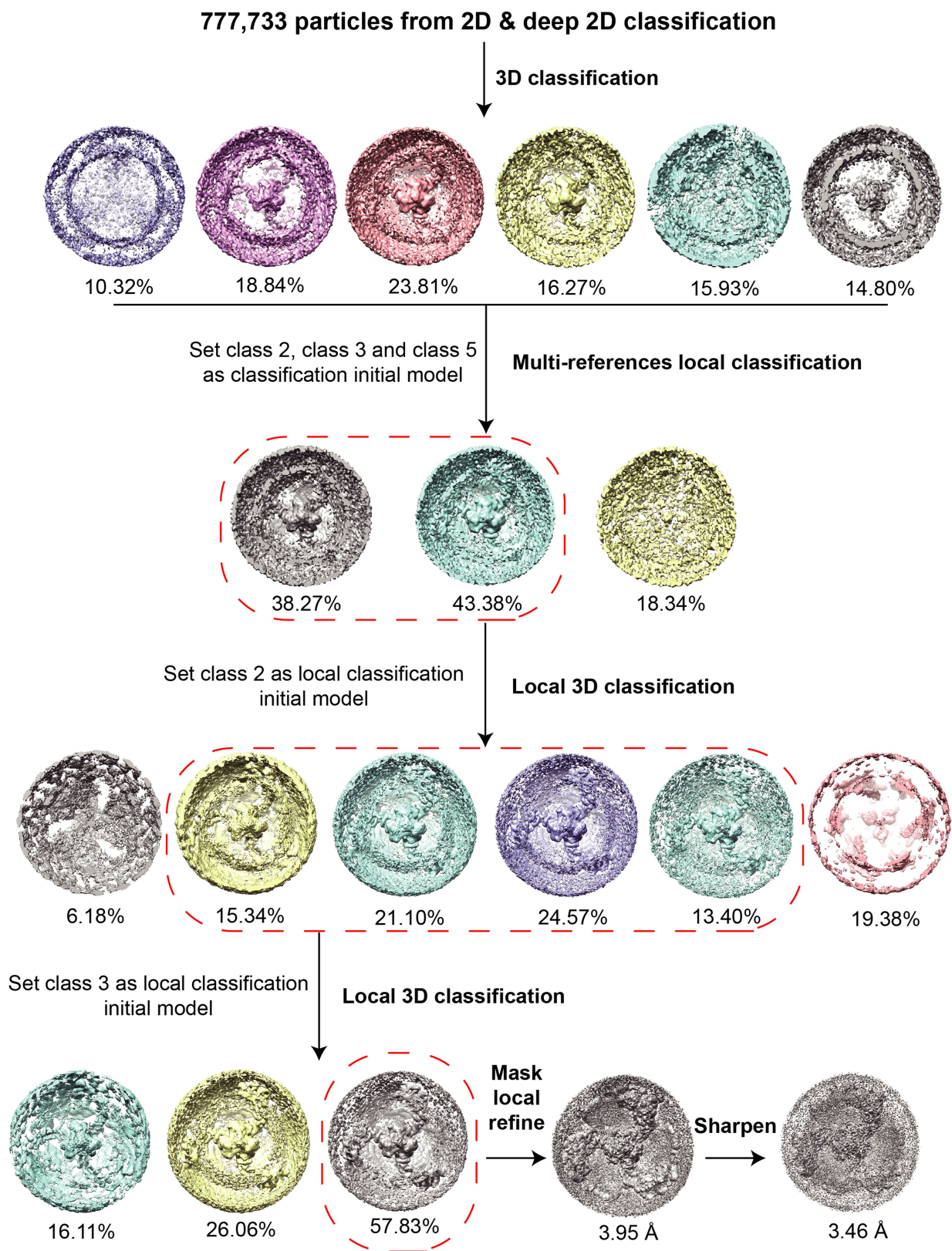
Extended Data Fig. 3 | See next page for caption.

Article

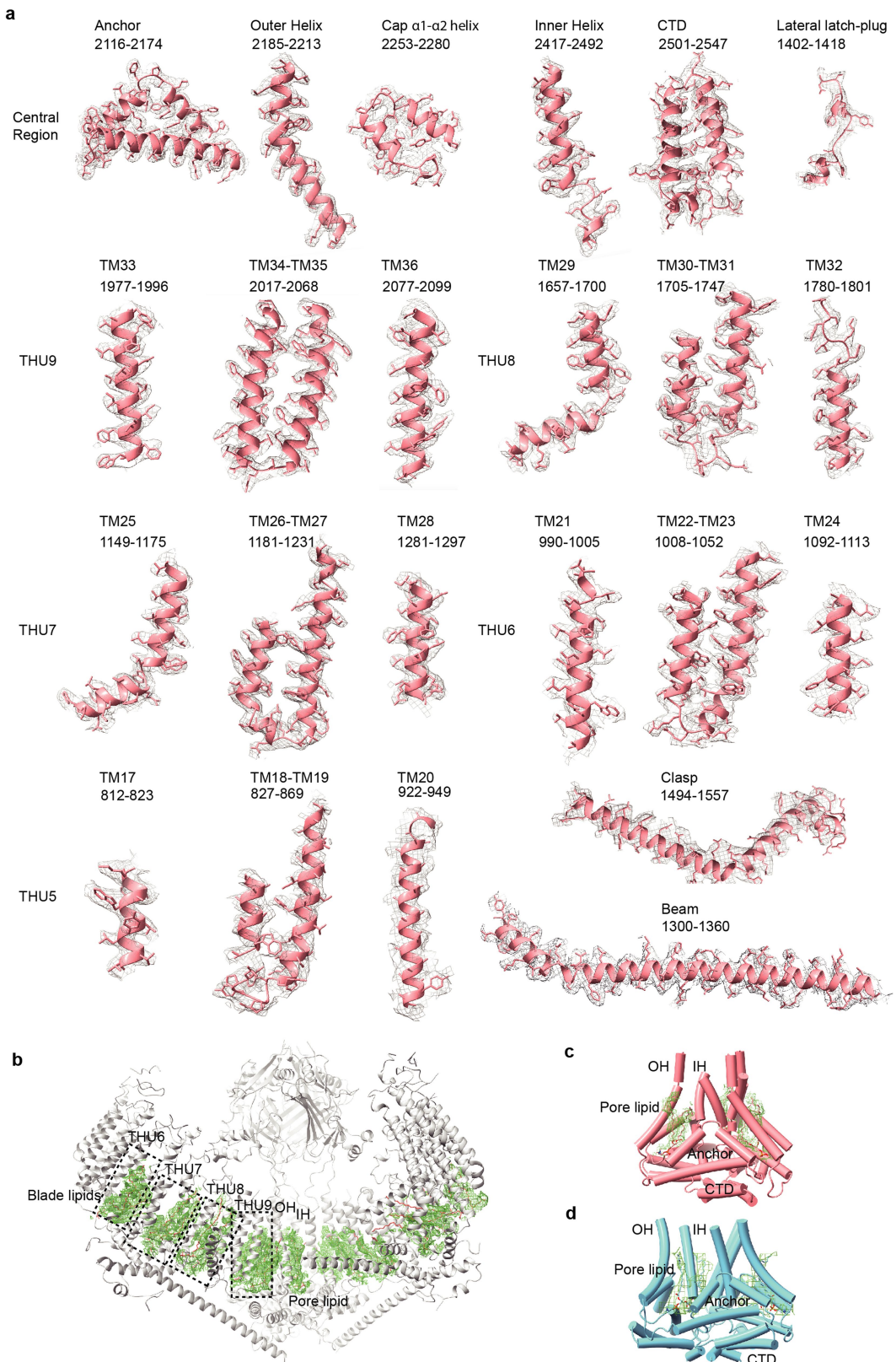
Extended Data Fig. 3 | Structural determination and analyses of the curved PIEZO1 structure derived from proteoliposomes.

a, 2D class averages of PIEZO1 proteoliposomes with a circular mask of 25 nm diameter, showing the cap domain located inside the vesicles. On the basis of the abruptly changed curvature, the red arrows might indicate the boundary between the PIEZO1-residing side and the opposite side lacking proteins. **b**, Local resolution maps of the curved PIEZO1 structure viewed from the top, side and bottom. **c**, Gold-standard Fourier shell correlation (FSC) curve of the indicated density map. The reported resolution was based on the FSC = 0.143 criteria. **d**, Side view of the 3D density map of the water-drop-shaped proteoliposome showing the resolved lipid bilayer and the embedded PIEZO1 at the indicated contour level. **e**, Cryo-EM map of the curved PIEZO1 structure derived from proteoliposomes at the contour level of 4 and 6. Compared to the density map resolved in detergent micelles (EMD: 6865) (**f**), the PIEZO1 map derived from proteoliposomes contains extra patches of densities in-between the blades and in parallel to the inner membrane layer. These densities are noticeable even at a high contour level of 4 and consist of the modeled α 1-helix of the clasp

domain (Clasp $^{\alpha 1}$), the α -helix preceding TM33 (TM33 $^{pre-\alpha 1}$), and potentially unmodeled intracellular loop regions that are stabilized by interacting with lipid layers. This layer of membrane-parallel structure might help to stabilize the bowl-shaped structure of PIEZO1 in lipid membranes. **f**, Cryo-EM map of the PIEZO1 structure derived from detergent micelles (EMD 6865) at the contour level of 6. **g**, The cartoon model of the curved PIEZO1 structure derived from proteoliposomes. The featured structural domains are labeled. The resolved blade lipids and pore lipids are shown in blue and green, respectively. **h**, Pore radius along the central axis of the ion conduction pathway of the indicated PIEZO1 structures derived from either detergent micelles (5Z10 and 6B3R) or the curved structure derived from proteoliposomes. The residues forming the TM gate and intracellular constriction neck are labeled. **i**, Surface presentation of the curved PIEZO1 structure colored based on lipophilicity, from gold (lipophilic) to blue (hydrophilic) and surface presentation of the blade lipids and the pore lipid enclosed in the dashed box, which is enlarged in the right box either in surface presentation or in cartoon model. The lateral portal is indicated by the red dashed box.

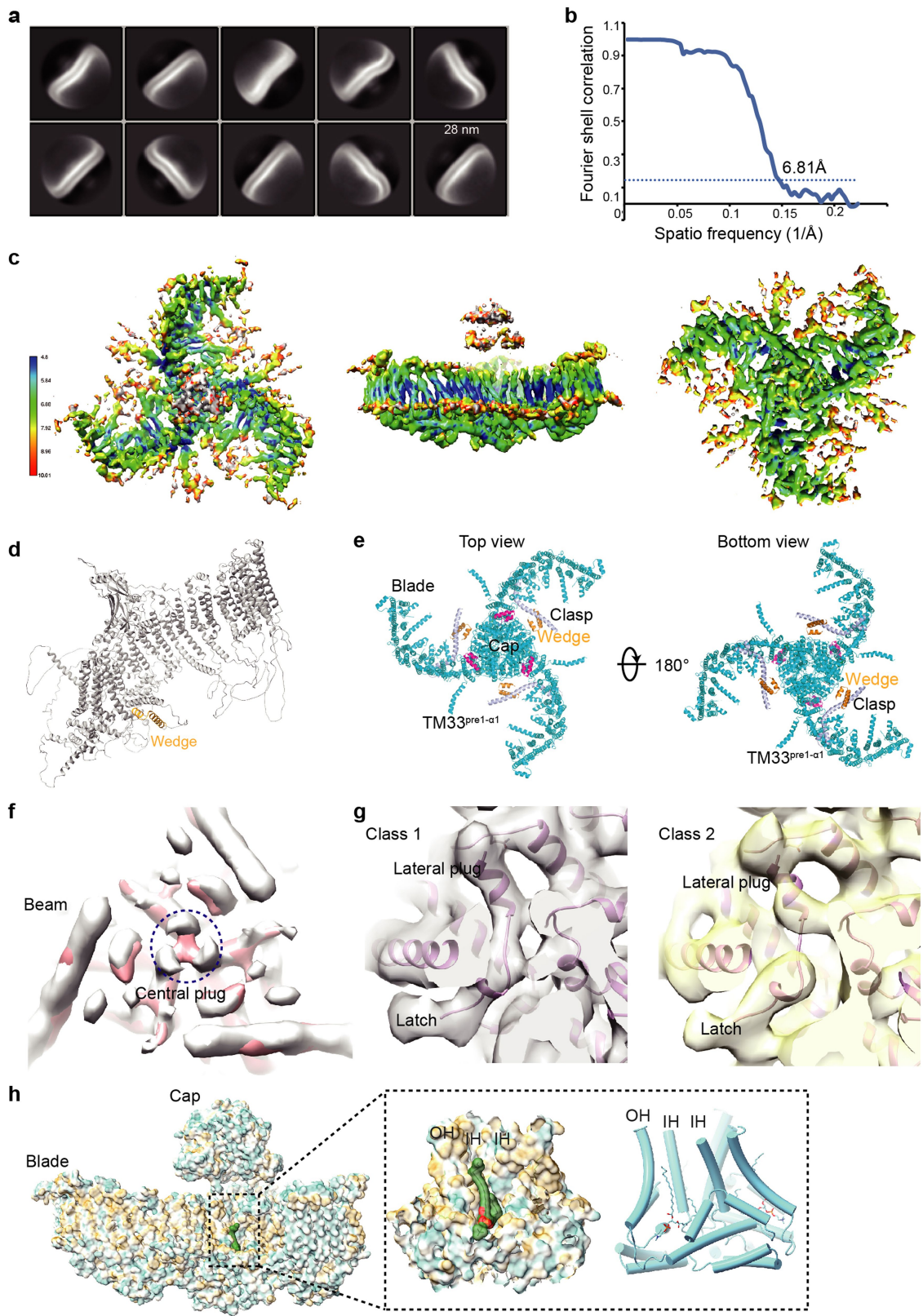


Extended Data Fig. 4 | Flowchart of EM data processing of the proteoliposomes with PIEZO1 being reconstituted in the outside-in configuration. Details of data processing were described in the Imaging processing part of Methods.



Extended Data Fig. 5 | Local EM density of the indicated domains of the curved PIEZO1 structure derived from proteoliposomes. **a**, The helices are shown in cartoon representation with side chains as sticks. The cryo-EM density is shown as gray mesh. **b**, A side view of the curved PIEZO1 structure

showing the blade lipid densities at the boundary of neighboring THU6 to THU9. **c** and **d**, A side view of the OH-IH enclosed central pore module showing the pore lipid densities either in the curved (**c**) or the flattened state (**d**).

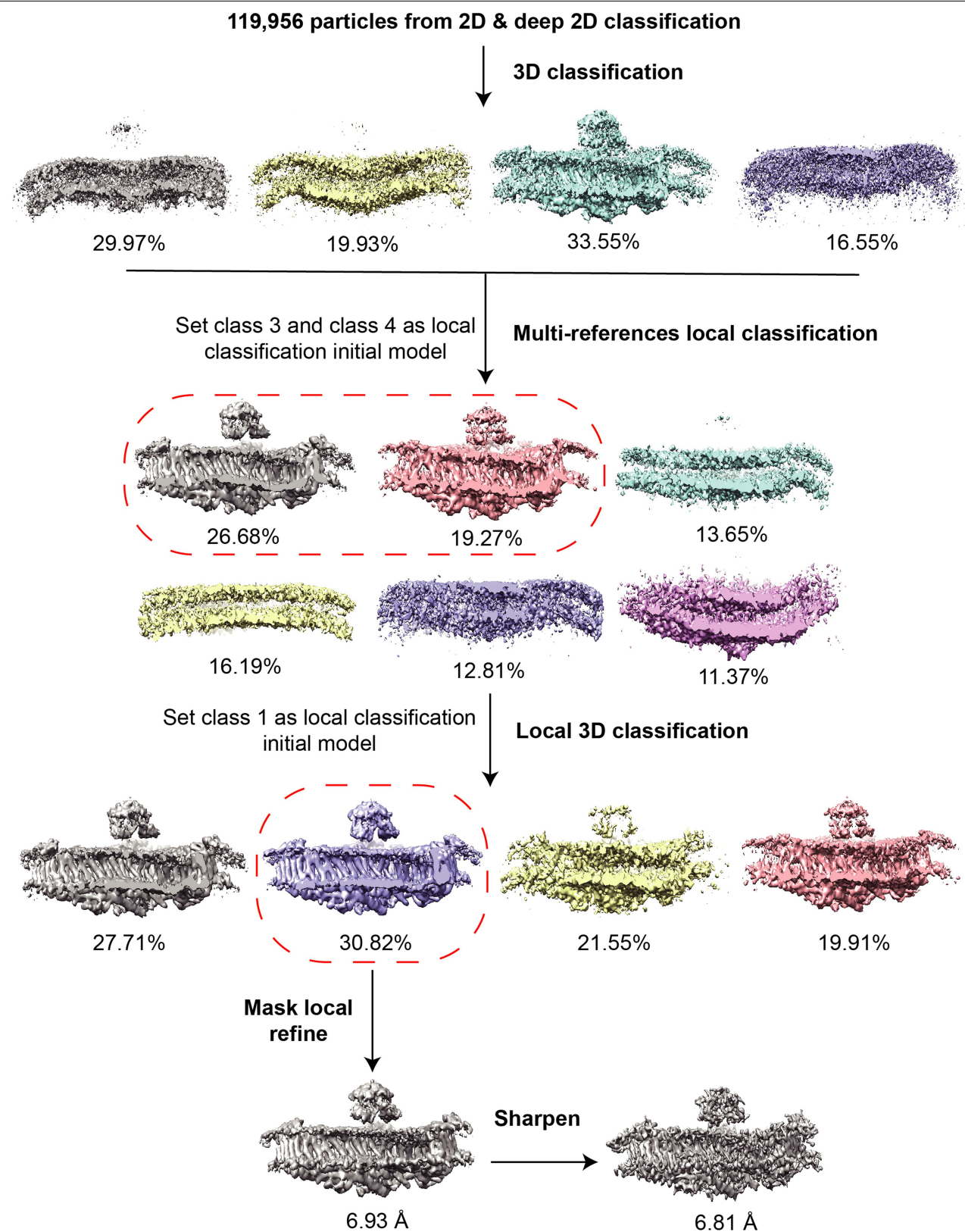


Extended Data Fig. 6 | See next page for caption.

Article

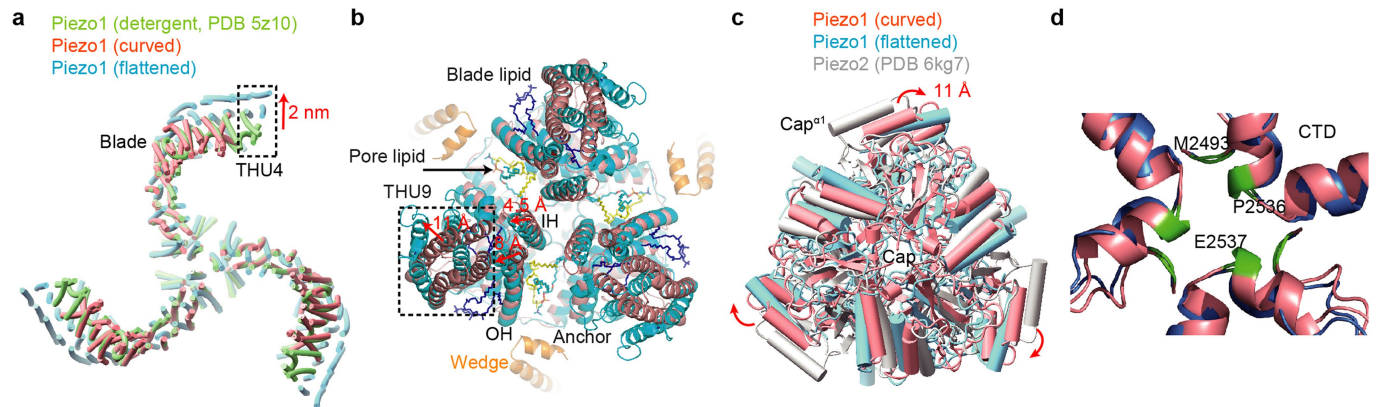
Extended Data Fig. 6 | Structural determination and analyses of the flattened PIEZO1 structure derived from proteoliposomes. **a**, 2D class averages of the D-shaped PIEZO1 proteoliposome vesicles with a circular mask of 28 nm diameter. **b**, Gold-standard Fourier shell correlation (FSC) curve of the flattened PIEZO1 structure. The reported resolution was based on the FSC = 0.143 criteria. **c**, Local resolution maps of the flattened PIEZO1 structure viewed from the top, side and bottom. **d**, The alphaFold2 predicted PIEZO1 structure with the wedge domain shown in orange. **e**, The indicated views of the cartoon model of the flattened PIEZO1 structure. The featured domains are

labeled. **f**, A bottom view of the overlaid curved and flattened cryo-EM maps showing the difference of the central plug density. **g**, A transparent view of the cryo-EM density of the lateral plug and latch domain showing the density variation of the lateral plug between 3D classified structures. **h**, Hydrophobic surface presentation of the flattened PIEZO1 structure and surface presentation of the pore lipid enclosed in the dashed box, which is enlarged in the right box either in the hydrophobic surface presentation or in cartoon model.



Extended Data Fig. 7 | Flowchart of EM data processing of the proteoliposomes with PIEZO1 being reconstituted in the outside-out configuration. Details of data processing were described in the Imaging processing part of Methods.

Article



Extended Data Fig. 8 | Structural comparisons. **a**, Top view of the superimposed PIEZO1 structures as indicated. For clarity, the extracellular cap and loops are omitted. The displacement of the THU4 is labeled. **b**, Top view of the superimposed central pore region of the curved and flattened PIEZO1 structures (salmon red and cyan, respectively). The wedge domain of the flattened structure is shown in orange. **c**, Top view of the superimposed cap of

the curved and flattened PIEZO1 structures (salmon red and cyan, respectively) and the PIEZO2 structure (PDB: 6KG7) (gray). The displacement of the Cap^{a1}-helix domain is labeled. **d**, A bottom view of the superimposed central pore of the curved and flattened structures of PIEZO1 showing the unchanged residues that form the intracellular constriction neck.

Extended Data Table 1 | Cryo-EM data collection, refinement and validation statistics**Cryo-EM data collection, refinement and validation statistics**

	#1 Curved state (EMDB-32592) (PDB 7WLT)	#2 Flattened state (EMDB-32593) (PDB 7WLU)
Data collection and processing		
Magnification	64,000	64,000
Voltage (kV)	300	300
Electron exposure (e-/Å ²)	50	50
Defocus range (μm)	-1.5~-2.4	-1.5~-2.4
Pixel size (Å)	1.098	2.196
Symmetry imposed	C3	C3
Initial particle images (no.)	3,572,926	3,772,712
Final particle images (no.)	209,166	35,012
Map resolution (Å)	3.46	6.81
FSC threshold	0.143	0.143
Map resolution range (Å)	6-2.4	10-4.8
Refinement		
Initial model used (PDB code)	5Z10/6B3R	5Z10/6B3R
Model resolution (Å)	3.5	7.5
FSC threshold	0.5	0.5
Map sharpening <i>B</i> factor (Å ²)	-55	-68
Model composition		
Non-hydrogen atoms	33912	34761
Protein residues	4059	4494
Ligands	27	3
<i>B</i> factors (Å ²)		
Protein	94.05	61.09
Ligand	106.88	71.78
R.m.s. deviations		
Bond lengths (Å)	0.011	0.009
Bond angles (°)	1.076	1.259
Validation		
MolProbity score	2.21	2.65
Clashscore	20.52	45.23
Poor rotamers (%)	0.89	0.27
Ramachandran plot		
Favored (%)	93.91	93.73
Allowed (%)	5.94	5.99
Disallowed (%)	0.15	0.27

Reporting Summary

Nature Portfolio wishes to improve the reproducibility of the work that we publish. This form provides structure for consistency and transparency in reporting. For further information on Nature Portfolio policies, see our [Editorial Policies](#) and the [Editorial Policy Checklist](#).

Statistics

For all statistical analyses, confirm that the following items are present in the figure legend, table legend, main text, or Methods section.

n/a Confirmed

- The exact sample size (n) for each experimental group/condition, given as a discrete number and unit of measurement
- A statement on whether measurements were taken from distinct samples or whether the same sample was measured repeatedly
- The statistical test(s) used AND whether they are one- or two-sided
Only common tests should be described solely by name; describe more complex techniques in the Methods section.
- A description of all covariates tested
- A description of any assumptions or corrections, such as tests of normality and adjustment for multiple comparisons
- A full description of the statistical parameters including central tendency (e.g. means) or other basic estimates (e.g. regression coefficient) AND variation (e.g. standard deviation) or associated estimates of uncertainty (e.g. confidence intervals)
- For null hypothesis testing, the test statistic (e.g. F , t , r) with confidence intervals, effect sizes, degrees of freedom and P value noted
Give P values as exact values whenever suitable.
- For Bayesian analysis, information on the choice of priors and Markov chain Monte Carlo settings
- For hierarchical and complex designs, identification of the appropriate level for tests and full reporting of outcomes
- Estimates of effect sizes (e.g. Cohen's d , Pearson's r), indicating how they were calculated

Our web collection on [statistics for biologists](#) contains articles on many of the points above.

Software and code

Policy information about [availability of computer code](#)

Data collection AutoEMation II, Serial EM

Data analysis MotionCor2,CTFFIND4.1,RELION-3.1,THUNDER, Resmap, IMOD4.7.9, EMAN2.2,Chimera,Chimera X, Coot 0.8.9, PHENIX1.18.2, HOLE, Pymol, AlphaFold2, MolProbity

For manuscripts utilizing custom algorithms or software that are central to the research but not yet described in published literature, software must be made available to editors and reviewers. We strongly encourage code deposition in a community repository (e.g. GitHub). See the Nature Portfolio [guidelines for submitting code & software](#) for further information.

Data

Policy information about [availability of data](#)

All manuscripts must include a [data availability statement](#). This statement should provide the following information, where applicable:

- Accession codes, unique identifiers, or web links for publicly available datasets
- A description of any restrictions on data availability
- For clinical datasets or third party data, please ensure that the statement adheres to our [policy](#)

The cryo-EM maps have been deposited in the Electron Microscopy Data Bank under accession codes 7WLT(curved) and 7WLU(flattened). The coordinates have been deposited in the Protein Data Bank under accession codes EMD-32592(curved) and EMD-32593(flattened). During structural analysis, PDB 5Z10, 6B3R, 6KG7, and EMD 6865 were used for comparison.

Field-specific reporting

Please select the one below that is the best fit for your research. If you are not sure, read the appropriate sections before making your selection.

Life sciences Behavioural & social sciences Ecological, evolutionary & environmental sciences

For a reference copy of the document with all sections, see nature.com/documents/nr-reporting-summary-flat.pdf

Life sciences study design

All studies must disclose on these points even when the disclosure is negative.

Sample size	Sample size was not predetermined for this study. Sample sizes of cryo-EM data were determined by the need to obtain meaningful structures and the availability of the microscope time.
Data exclusions	Micrographs with poor qualities (astigmatism, image drift, ice contamination) were excluded from the datasets. Particles in 2D classes showing no secondary structural features and in 3D classes showing unsatisfactory structural features were excluded from the final reconstructions.
Replication	Piezo1 proteoliposome purification and reconstitution were successfully done in biological replicates for more than 10 times. For cryo-EM, 6 datasets from 6 parallel preps were collected independently. All attempts were successful for cryo-EM experiments.
Randomization	In the 3D refinement, all particles were randomly split into two half groups, one for refinement and the other for validation. During Piezo1 reconstitution and data collection, we did not allocate experimental groups thus no randomization was required for those experiments.
Blinding	The investigators were not blinded because blinding is not practically feasible and applicable to structure determination by cryo-EM.

Reporting for specific materials, systems and methods

We require information from authors about some types of materials, experimental systems and methods used in many studies. Here, indicate whether each material, system or method listed is relevant to your study. If you are not sure if a list item applies to your research, read the appropriate section before selecting a response.

Materials & experimental systems

n/a	Involved in the study
<input checked="" type="checkbox"/>	Antibodies
<input type="checkbox"/>	Eukaryotic cell lines
<input checked="" type="checkbox"/>	Palaeontology and archaeology
<input checked="" type="checkbox"/>	Animals and other organisms
<input checked="" type="checkbox"/>	Human research participants
<input checked="" type="checkbox"/>	Clinical data
<input checked="" type="checkbox"/>	Dual use research of concern

Methods

n/a	Involved in the study
<input checked="" type="checkbox"/>	ChIP-seq
<input checked="" type="checkbox"/>	Flow cytometry
<input checked="" type="checkbox"/>	MRI-based neuroimaging

Eukaryotic cell lines

Policy information about [cell lines](#)

Cell line source(s)	HEK293T
Authentication	The cell line used was not authenticated.
Mycoplasma contamination	Negative
Commonly misidentified lines (See ICLAC register)	No commonly misidentified cell lines were used.